Watching Excited State Dynamics with Optical and X-ray Probes: The Excited State Dynamics of Aquocobalamin and Hydroxocobalamin.

Roseanne J. Sension[1,2]*, Taylor P. McClain[3], Ryan M. Lamb[1], Roberto Alonso-Mori[4], Frederico Alves Lima[5], Fernando Ardana-Lamas[5], Mykola Biednov[5], Matthieu Chollet[4], Taewon Chung[1], Aniruddha Deb[1,3], Paul A. Dewan Jr.[3], Leland B. Gee[4], Joel Huang Ze En[1], Yifeng Jiang[5], Dmitry Khakhulin[5], Jianhao Li[1], Lindsay B. Michocki[1], Nicholas A. Miller[1], Florian Otte[5], Yohei Uemura[5], Tim B. van Driel[4], James E Penner-Hahn[1,3]*

[1]Department of Chemistry, University of Michigan, 930 N University Ave. Ann Arbor, Michigan, 481091055, U.S.A.

[2]Department of Physics, University of Michigan, 450 Church Street, Ann Arbor, Michigan, 48109-1040, U.S.A.

[3]Biophysics, University of Michigan, 930 N University Ave. Ann Arbor, Michigan, 48109-1055, U.S.A.

[4]Linac Coherent Light Source, SLAC National Accelerator Laboratory, 2575 Sand Hill Road, Menlo Park, CA 94025, U.S.A.

[5]Femtosecond X-ray Experiments Group, European XFEL, Holzkoppel 4, 22869 Schenefeld, Germany,

*Corresponding Authors e-mail: rsension@umich.edu, Phone: 734-763-6074; jeph@umich.edu

ABSTRACT

Femtosecond time-resolved X-ray absorption (XANES) at the Co-K-edge, X-ray emission (XES) in the Co-Kβ and valence-to-core region, and broadband UV-vis transient absorption are combined to probe the femtosecond to picosecond sequential atomic and electronic dynamics following photoexcitation of two vitamin B_{12} compounds, hydroxocobalamin and aquocobalamin. Polarized XANES difference spectra allow identification of sequential structural evolution involving first the equatorial and then the axial ligands with the latter showing rapid coherent bond elongation to the outer turning point of the excited state potential followed by recoil to a relaxed excited state structure. Time-resolved XES, especially in the valence-to-core region, along with polarized optical transient absorption suggests that the recoil results in formation of a metal-centered excited state with a lifetime of 2-5 picoseconds. This combination of methods provides a uniquely powerful tool to probe the electronic and structural dynamics of photoactive transition metal complexes and will be applicable to a wide variety of systems.

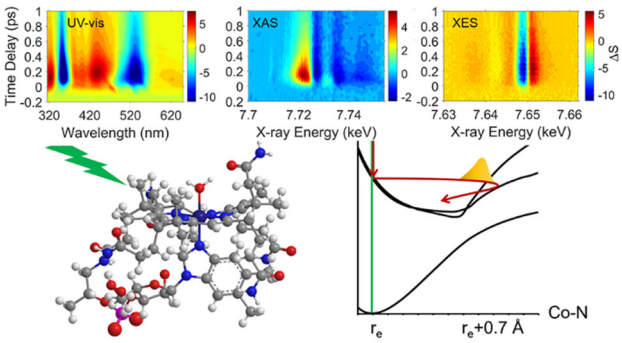

INTRODUCTION

Cyclic metal-centered tetrapyrroles comprise an important class of cofactors that includes the porphyrins, hemes, chlorins, and corrins. These are widely utilized both in biological systems and in synthetic chemistry. The reactions of these molecules exploit changes in oxidation state, spin state, axial ligation, and electronic structure. In addition to their ground state reactivity, the strong optical absorption of the conjugated ring has led to a variety of photochemical applications ranging from light harvesting and energy conversion to photodynamic therapy, gene regulation, and drug delivery.[1-9] Ultrafast transient absorption spectroscopy in the visible and ultraviolet regions of the spectrum has proven to be an invaluable tool in the study of these photochemical transformations. Unfortunately, UV-visible transient absorption spectra can be ambiguous to interpret and do not typically provide a direct link to molecular structure. As a consequence, while time scales can be exquisitely well defined using UV-visible transient absorption spectroscopy, the connection to electronic and structural dynamics is often less clear.[10-15] Ultrafast X-ray spectroscopies offer an *element specific* probe of these dynamics, helping to refine assignments and thus providing new understanding of the structural transformations that occur following photoexcitation.[16-23] In this paper we use ultrafast X-ray absorption at the Co K-edge and ultrafast X-ray emission in the $K\beta_{1,3}$ and valence-to-core regions to probe the excited state dynamics of two cobalamin compounds and use the results to obtain insights into the excited state dynamics.

Cobalamin compounds are of increasing interest, both for their biological function and their synthetic potential. Enzymatic reactions of coenzyme B_{12} (adenosylcobalamin, AdoCbl) and methylcobalamin (MeCbl) are essential for human health and well-being.[24,25] As a consequence, the ground state chemistry of cobalamins has been investigated extensively. More recently, the significance of the photochemistry of cobalamins has been realized with applications exploiting

both the photolability of alkylcobalamins and the photostability of non-alkylcobalamins such as aquo, hydroxo, and cyanocobalamin (H_2OCbl^+, HOCbl, CNCbl).

Chemical reactivity is controlled by the coupled dynamics of electrons and nuclei. The photochemical and photophysical pathways accessed in cobalamins are determined by seams of intersection between several low-lying electronically excited states.[26-28] Structural deformations coupled with changes in electronic configuration facilitate internal conversion and relaxation. While alkylcobalamins are generally photolabile, resulting in cleavage of the Co-C bond on a sub nanosecond time scale, this can be modified by the environment and by the nature of the alkyl ligand.[29-32] In fact, control of the photochemistry of AdoCbl is vital to the sensing function of the B_{12} dependent photoreceptor, CarH.[7,33-38]

In contrast with the photolability of alkylcobalamins, non-alkylcobalamins are generally photostable. Channels for rapid internal conversion to the ground electronic state compete effectively with bond dissociation and radical pair formation. Cyanocobalamin (vitamin B_{12}, CNCbl) is the most commonly isolated form of the cofactor. The quantum yield for photolysis of CNCbl in solution is vanishingly small, although triplet mechanisms for photodegradation of the solid have been reported.[39] Internal conversion to the ground state occurs on a picosecond time scale dependent on solvent polarity and temperature.[40,41] Both aquocobalamin (H_2OCbl^+, vitamin B_{12a}, Figure 1) and hydroxocobalamin (HOCbl, vitamin B_{12b}) are photostable under visible and near-UV excitation, although bond homolysis is observed with excitation wavelengths shorter than 300 nm.[11,42] The photostability of H_2OCbl^+ and HOCbl is essential to the gene regulation function of the AeR proteins.[43-46] In addition to this natural biological function, cobalamins also provide a promising platform in optogenetics,[34,35,47] as light-activated agents for spatially and temporally controlled delivery of therapeutic agents,[8,9] and as a biocompatible scaffold for CO releasing metal

carbonyls.[48,49] Thus, the factors controlling the photochemistry of cobalamins are also of significant practical interest.

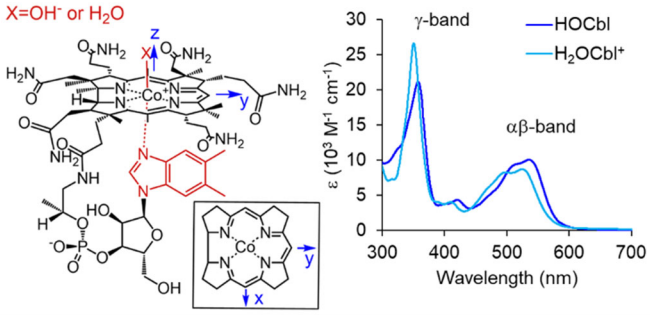

Figure 1. Left) Schematic illustration of the structure of HOCbl and H_2OCbl^+, showing the molecular coordinate system used in this work (inset gives a truncated view of the ring looking down the z axis). Right) UV-visible absorption spectra of HOCbl and H_2OCbl^+.

Detailed understanding of the nature of the coupled electronic and atomic degrees of freedom responsible for the observed photochemistry and photophysics of cobalamins remains elusive. Ultrafast UV-Visible spectroscopy (Transient absorption or TA) allows the monitoring of valence electronic and coupled vibrational changes with exceptional time resolution and sensitivity. However, interpretation of these data can be challenging. While coherent oscillations will sometimes reveal details about the vibrational motions that are coupled to the excitation, it is more often the case that structural dynamics can only be inferred indirectly. Moreover, the use of visible light for both excitation and probing means that the earliest processes (<100 fs) are often obscured by coherent features arising from interactions of the pump and probe beams, but unrelated to the photochemistry and photophysics of interest.

The UV-visible transient absorption spectra of both H_2OCbl^+ and HOCbl for a range of excitation wavelengths were reported earlier.[11] These data were modeled using a global analysis fit to a sum of exponentials yielding a fast component (0.35 ± 0.15 ps, H_2OCbl^+ and 0.30 ± 0.10

ps, HOCbl), and a small amplitude picosecond decay (2.3 ± 0.3 ps, H_2OCbl^+ and 5.3 ± 0.4 ps, HOCbl). The identification of additional faster components, <100 fs, in these data was complicated by the limited time-resolution and the presence of coherent features (eg. cross phase modulation, two-photon absorption, and stimulated Raman scattering), but are now identified in the X-ray measurements (see below). Thus, both species show evidence for three different excited state species or evolution associated populations consistent with a model $\mathbf{S_0 \rightarrow A \rightarrow B \rightarrow C \rightarrow S_0}$ where **A** represents the initial (Franck-Condon) excited state, which decays first to a population **B**, then to **C**, and then ultimately to the ground state. Despite that broad similarity in temporal behavior, the spectral changes for H_2OCbl^+ and HOCbl were different. In particular, the absence of clean isosbestic points for H_2OCbl^+ suggested that this species relaxed through rapid (0.35 ps) formation of a vibrationally hot ground state which thermally equilibrated over the next several ps, while HOCbl relaxed first to a relatively long-lived (5 ps) excited electronic state, which then underwent internal conversion to the ground state. These observations, together with theoretical calculations suggesting a pathway for rapid internal conversion for H_2OCbl^+ but not for HOCbl,[11] led to the hypothesis of distinct photophysical pathways for the two molecules.

With the development of femtosecond X-ray free electron lasers (XFELs), it has become possible to interrogate directly the coupled electronic and structural changes that are responsible for chemical transformations, and to do so on femtosecond time scales and with element-specific sensitivity. Photoactive transition metal compounds provide a particularly fruitful system for the application of ultrafast X-ray methods. Polarized time-resolved X-ray absorption (tr-XAS) in the X-ray absorption near edge structure (XANES) region is sensitive to the scattering of the X-ray excited photoelectron by nearby atoms, and thus can be used to study sequential structural dynamics of cobalamins and other compounds.[21,22] In contrast, XAS features in the pre-edge region

and X-ray emission (XES) can be described as bound-state transitions and are thus more sensitive to details of the electronic structure. Time-resolved X-ray emission (tr-XES) and tr-XAS can thus be used to probe both the electronic and structural dynamics of the photoexcited cobalt.[13,50-56] Combined, these methods provide a powerful probe of photochemical dynamics. In prior studies, we used tr-XANES at the cobalt K-edge to probe the excited state dynamics of AdoCbl and CNCbl.[21-23] Here, we combine cobalt K-edge tr-XAS in the pre-edge and XANES regions with cobalt Kβ and valence-to-core tr-XES to probe the femtosecond and picosecond electronic and structural dynamics of H_2OCbl^+ and HOCbl. The focus of our studies is on the initial coherent wave packet motion and on the mechanisms for ground state recovery in these two compounds. Our XANES and XES measurements suggest that both molecules exhibit similar excited state dynamics, differing in time scale, but not in mechanism.

RESULTS

XANES

Time-resolved XANES spectra of H_2OCbl^+ and HOCbl following 520 nm excitation were obtained for time delays between -0.4 ps and 2 ps. The isotropic difference spectra are plotted in Figure 2. Both compounds exhibit a large transient signal that decays to a much smaller signal within half a picosecond. For HOCbl, a high potassium concentration and small number of scans results in a much lower signal-to-noise ratio. However, the general trends are the same.

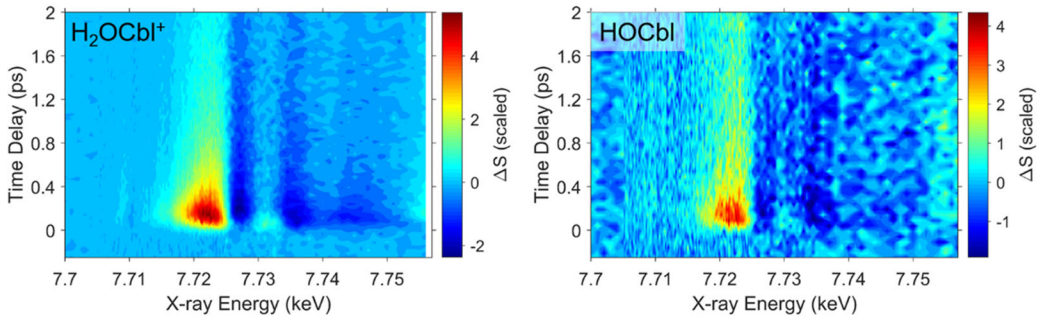

Figure 2. Isotropic tr-Co-XANES difference spectra for H_2OCbl^+ (left) and HOCbl (right).

The tr-XANES data are consistent with the presence of at least 3 distinct excited state species: an initial ππ* excited state produced immediately upon optical excitation that will be designated "**A**" identified by the positive difference signal around 7.73 keV at the very earliest times; a population present at ca. 150-200 fs corresponding to the maximum of the transient signal that will be designated "**B**"; and a longer-lived state that will be designated "**C**" with a lifetime of ca. 2.3 ps for H_2OCbl^+ and 5.3 ps for HOCbl. An estimate of the excitation fraction, *f*, permits the reconstruction of the corresponding excited state spectra from the isotropic difference spectrum ΔS_{Total} as defined in Eq. 1.

$$\Delta S_{Total} = \Delta S_{\parallel} + 2\Delta S_{\perp}$$
$$S_{ES} = \frac{\Delta S_{Total}}{3f} + S_{GS} \quad (1)$$

The excitation fraction is estimated as f=0.4 for H_2OCbl^+ and 0.5 for HOCbl (see Experimental Methods and SI for more detail). The evolution of the excited state spectra and the estimated spectra for each population, **A**, **B**, and **C**, are illustrated in Figure 3.

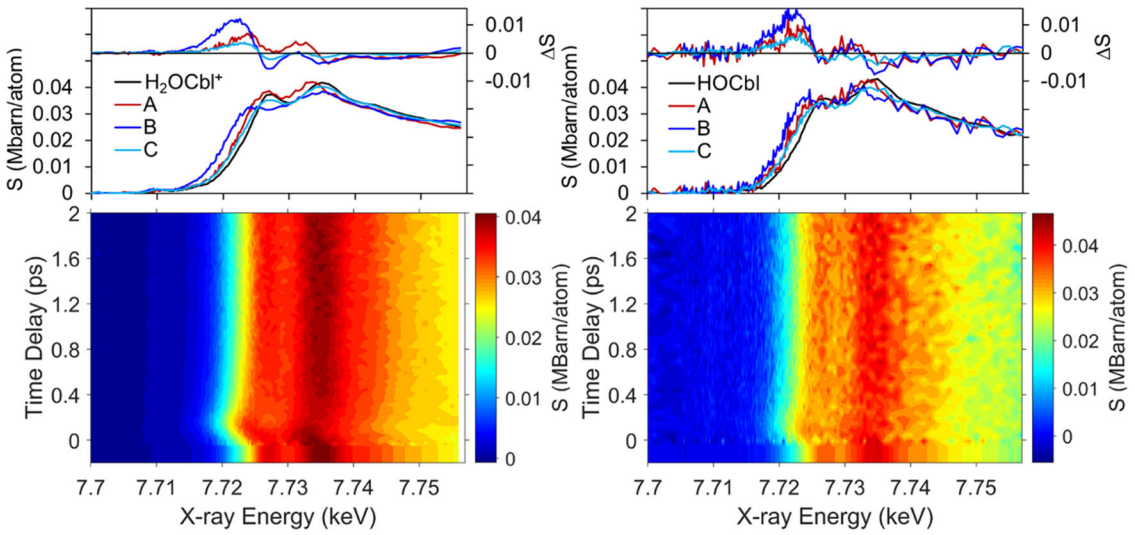

Figure 3. Evolution of the XANES spectrum as a function of time. The surface plots in the lower

panels illustrate the motion of the Co XANES edge. The upper panels illustrate the isotropic difference spectra, the ground state XANES spectrum, and the estimated excited state XANES spectra at the earliest time delays (**A**), at ca. 150 to 200 fs (**B**) and of the species with a picosecond lifetime (**C**).

The signals obtained for parallel and perpendicular polarization geometries allow us to distinguish the structural changes that occur along the direction of the initially excited transition dipole (defined as the molecular *x*-axis) from those that occur in the orthogonal directions.[10,21-23]

$$\begin{aligned} \Delta S_x &= 2\Delta S_{\parallel} - \Delta S_{\perp} \\ \Delta S_{y+z} &= 3\Delta S_{\perp} - \Delta S_{\parallel} \end{aligned} \tag{2}$$

The optical pulse energy for the measurements on H_2OCbl^+ was higher than desired for optimal polarization discrimination and the data were therefore corrected for imperfect polarization discrimination (See the Experimental Methods section as well as additional discussion in SI including Figures S8 and S9). Measurements made earlier with much lower optical pulse intensity confirm the validity of this correction (Figure S9). As illustrated in Figure 4, the initial transient, **A**, is confined primarily to the ring. There is a small difference signal polarized in *x* and similarly sized signal in *y*+*z*. While *y* and *z* cannot be distinguished experimentally, the approximate 4-fold symmetry of the corrin argues in favor of the initial *y*+*z* transient in **A** arising primarily from *y*-polarized distortions, with the similar amplitude suggesting that there are equal *x*- and *y*-polarized contributions. In contrast, species **B** is characterized by a large increase in the *y*+*z*-component. This demonstrates that **B** is dominated by expansion of one or both axial bonds. The picosecond-lived state **C** is characterized by smaller differences in the axial direction and almost no *x*-polarized contribution suggesting that the ring has returned nearly to the ground-state structure in **C**. The data for HOCbl plotted in Figure 4 were obtained using a lower optical pulse energy. As a result, the excitation fraction is smaller (f=0.25) and the polarization discrimination is better than for

H_2OCbl^+, although noise from potassium scattering complicates the analysis. The data available for HOCbl does not permit decomposition into direction dependent contributions at the earliest times (species **A**), but the trends at longer time delays are similar for the two molecules.

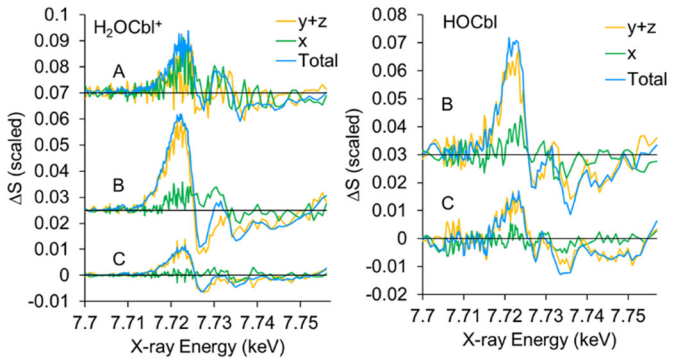

Figure 4. The polarization decomposition for the tr-Co-XANES observed following excitation of H_2OCbl^+ and HOCbl. The data for HOCbl does not permit decomposition into direction dependent contributions for the initial species designated **A**. The excitation fraction for H_2OCbl^+ was ca. 0.4 and as a result the polarization discrimination is imperfect. A correction was applied in the left hand column of Figure 4 (See SI discussion and Figure S9). The excitation fraction for the HOCbl data plotted here was ca. f=0.25 and a correction is unnecessary.

XAS Pre-Edge Region

Qualitatively, the pre-edge region of H_2OCbl^+ shows two resolved transitions, a relatively strong feature at ~7710.1 eV and a broad weaker feature ~ 5 eV higher energy. The intensity of the first feature is higher than would typically be expected for an approximately octahedral Co site. The larger ground state pre-edge transition for H_2OCbl^+ peaking at 7710.1 eV is approximately Gaussian in lineshape with a FWHM of 1.8 eV, consistent with the convolution of the intrinsic 1s core-hole width (ca. 1.25 eV) and estimated spectrometer resolution (ca. 1.5 eV). In order to shed light on the origin of these features, we have used TDDFT calculations of the spectra; in previous work, transitions in this region have been well modeled by TDDFT calculations.[57-60] For comparison with the experimental spectrum, an energy shift of 17.1 eV was used to match the

observed energy of the primary pre-edge transition and a 1.77 eV FWHM Gaussian lineshape was used for all transitions (Figure 5). The calculations suggest that there are three main contributions to the observed spectrum. At the lowest energy there is a $1s \rightarrow \sigma^* 3d_{z^2} / \pi^*$ transition and ~1.3 eV higher in energy an unresolved $1s \rightarrow 3d_{xy} / \pi^*$ transition (see Figs. 1 and 6 for a discussion of coordinate system). The former has significant dipole character as a result of 4p$_z$ mixing into the final state and is predicted to be polarized in the *z*-direction. In contrast, the latter has almost exclusively quadrupole character. The dipole character of the first transition accounts for the unusually intense pre-edge spectra. Approximately 4.7 eV higher in energy there are again two unresolved transitions, a very weak $1s \rightarrow \sigma^* 3d_{z^2} / \pi^*$ transition and a second $1s \rightarrow 3d_{xy} / \pi^*$ transition, but this time an in-phase combination of LUMO+2 and LUMO+3. The latter transition gains intensity from 4p mixing and is predicted to have significant *x*, *y*, and *z* components to the transition dipole. The simulation agrees reasonably well with the measured spectrum as shown in Figure 5, including agreement with the presence of two clear peaks and the separation between these peaks.

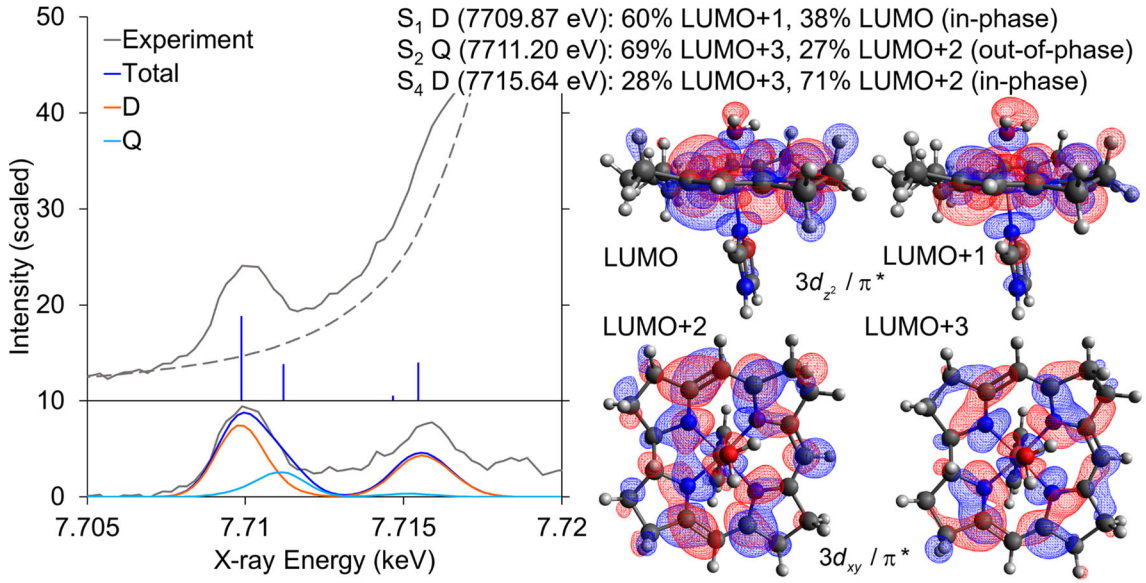

Figure 5. Experimental and simulated Co pre-edge transitions for H_2OCbl^+. The baseline under the pre-edge transitions is estimated and subtracted from the data as shown to allow better comparison with the calculated spectrum. The structural parameters for the ground state are discussed in more detail with the XANES simulations below. Note that the designation $3d_{xy}$ for the unoccupied approximately e_g orbital, rather than the more traditional $3d_{x^2-y^2}$, is a consequence of the fact that we have defined *x* as the transition dipole moment direction for the visible transition and, as illustrated in Figure 1, this falls between the equatorial Co-N bonds rather than along these bonds. A similar figure for HOCbl is included in SI (Figure S10).

The time-resolved X-ray absorption signal in the pre-edge region of H_2OCbl^+ is consistent with a significant change in structure and/or electronic configuration for both species **B** and **C** (Figure 6). The transition for species **B** is also approximately Gaussian with a FWHM of 1.8 eV, but with a lower intensity than the ground state and is red-shifted to ca. 7709.3 eV. The pre-edge transition for state **C** is approximately Gaussian in lineshape with the same width and intensity as the ground state transition, but with a peak at an intermediate energy of ca. 7709.8 eV. The pre-edge signal is weak, precluding a reliable decomposition into components *x* and *y*+*z*. The time traces on the right hand side of Figure 6 are consistent with three dynamic species. There is a rapid bleach around 7710.3 eV accompanied by an increase in absorption around 7708 eV and 7712 eV. These all show rapid decay over a few hundred fs, accompanied by a delayed increase in absorption around 7709.4 eV. Finally, there is a longer-lived species exhibiting a small increase in absorption at all of these energies.

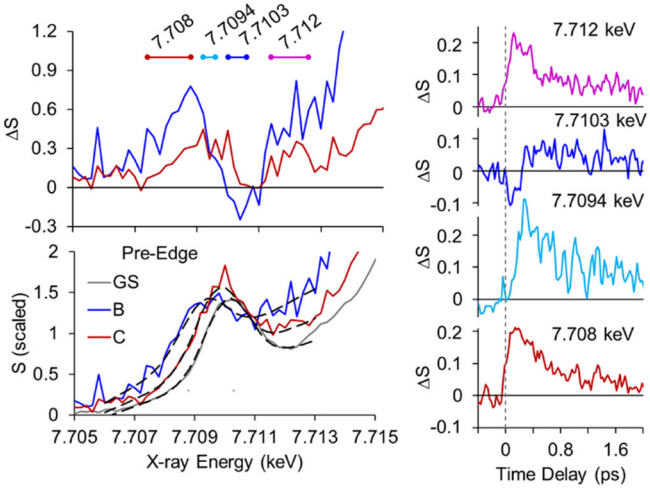

Figure 6. Left: Isotropic difference spectra and estimated excited state spectra in the Co pre-edge region for species **B** and **C** following excitation of H_2OCbl^+. The horizontal bars in the upper panel indicate the energy ranges that were integrated to follow the time-evolution of the signal (right panel). The ground and estimated excited state spectra in the lower panel are fit to Gaussian line shapes as described in the text. These fits are indicated black dashed lines. Right: The time-dependence of the tr-XAS signal averaged over the energy ranges indicated by the horizontal bars in the upper left panel. The central energy for each range is indicated.

X-ray Emission

Time-resolved $K\beta_{1,3}$ X-ray emission spectra were obtained following 400 nm excitation of both H_2OCbl^+ and HOCbl (Figure 7a,b). The isotropic UV-visible difference spectra following excitation at 400 nm are similar to those obtained following excitation in the αβ band between 530 nm and 575 nm.[11] Coherent features prevent comparisons at early times (<100 fs), but the kinetic traces are independent of excitation wavelength at longer time delays (see Figures S6 and S7) suggesting similar excited state dynamics following excitation. At least three distinct species are revealed in the transient XES data (see Figure S2). The change in the XES band at the very earliest time (species **A**) is characterized by a small red-shift as illustrated in Figure 7d. It is possible that the nature of this initial state may depend on excitation wavelength (although see below); however,

the identity of later-time UV-visible TA results demonstrates that the later species (>~150 fs) are independent of excitation wavelength (See Figure S6). The XES for the excited state species designated **B** is characterized by a blue-shift of the main emission band and an increase in the emission intensity around 7.638 keV. The effect is significantly larger for H_2OCbl^+ than for HOCbl. In contrast to this difference at short times, the changes in the XES for the longer-lived state **C** are approximately the same for both molecules.

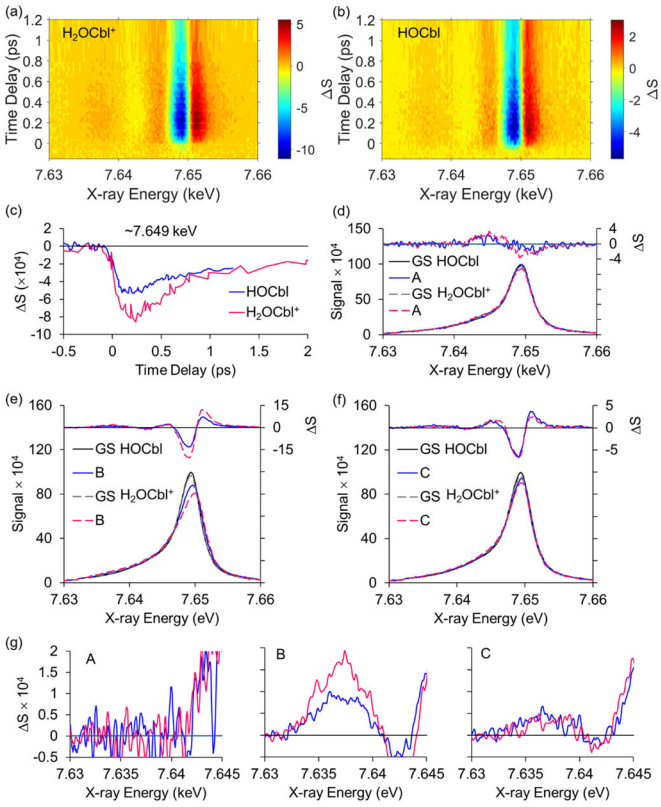

Figure 7. Tr-XES measurements of the Co $K\beta_{1,3}$ emission band following 400 nm excitation. (a) and (b) Surface plots of the time-dependent difference spectra for H_2OCbl^+ and HOCbl, respectively. (c) The time-dependent reduction and recovery of the $K\beta_{1,3}$ main-line emission band for H_2OCbl^+ and HOCbl. Panels (d), (e) and (f) compare the difference spectra and estimated XES spectra of H_2OCbl^+ and HOCbl for species A, B, and C. (g) The absorption increases in the region often designated Kβ′ are compared for both molecules and all three species. The color key is the same as in panel (c).

In a separate series of measurements, time-resolved $K\beta_{1,3}$ XES spectra of both H_2OCbl^+ and HOCbl were obtained following 550 nm excitation. For these measurements, the detector was positioned to cover the valence-to-core region between 7.680 keV and 7.720 keV and as a result the $K\beta_{1,3}$ region was limited to energies >7.644 keV. Thus, the region often designated Kβ′ that is highlighted in Figure 7(g) was not included in these measurements. Transient spectra were measured for time delays between -400 fs and 1 ps. The transient spectra were also measured at set time delays of 200 fs and 1 ps to improve the signal-to-noise ratio for the weak valence-to-core transition. These results are summarized in Figure 8. The overall dynamics in the $K\beta_{1,3}$ region are similar to those observed following 400 nm excitation.

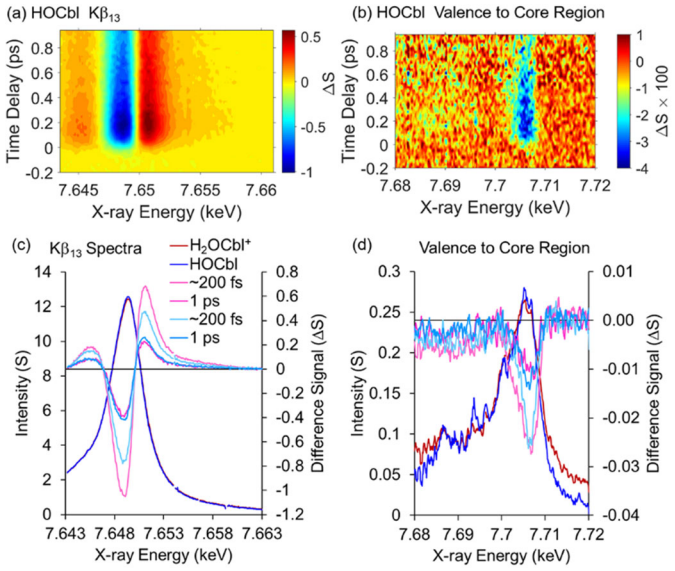

Figure 8. Tr-XES measurements of the Co $K\beta_{1,3}$ and valence-to-core emission bands of H_2OCbl^+ and HOCbl following 550 nm excitation. (a) and (b) Surface plots of the time-dependent difference spectra for HOCbl in the $K\beta_{1,3}$ and valence-to-core bands. The valence-to-core region for H_2OCbl^+ is plotted in Fig. S11(a). (c) Comparison of the ground state $K\beta_{1,3}$ XES with the difference signals obtained at ca. 200 fs and at 1 ps. (d) Comparison of the ground state valence-to-core emission bands with the difference signals obtained at ca. 200 fs and at 1 ps. The legend is the same as in panels (c)

and (d).

The transient difference spectra obtained for both H_2OCbl^+ and HOCbl following 550 nm excitation were fit to a model consisting of a sum of three exponential decay components. The lifetime of the initial state was fixed at 50 fs, consistent with the XANES measurements described above. The lifetime of the femtosecond species **B** was allowed to vary freely. Because the time-resolved emission spectrum was only measured out to 1 ps, the lifetime of the picosecond state was fixed at the lifetimes obtained from the UV-visible transient absorption measurements, i.e. 2.3 ps for H_2OCbl^+ and 5.3 ps for HOCbl. The lifetimes obtained from this fit for the intermediate state **B** are 0.34 ps for H_2OCbl^+ and 0.25 ps for HOCbl, consistent with the values obtained from the UV-visible TA measurements (0.35 ± 0.15 ps, H_2OCbl^+ and 0.30 ± 0.10 ps, HOCbl). The species associated difference spectra calculated using a sequential model are plotted in Figure 9 (a) and (b). Kinetic traces averaged over significant spectral regions are plotted with the fits in Figures 9 (c) and (d). The fastest transient signal is observed in the valence-to-core region (δ) and on the low-energy wing of the $K\beta_{1,3}$ transition (α). The blue-shift of the $K\beta_{1,3}$ mainline (β, γ) is delayed, peaking around 150 fs.

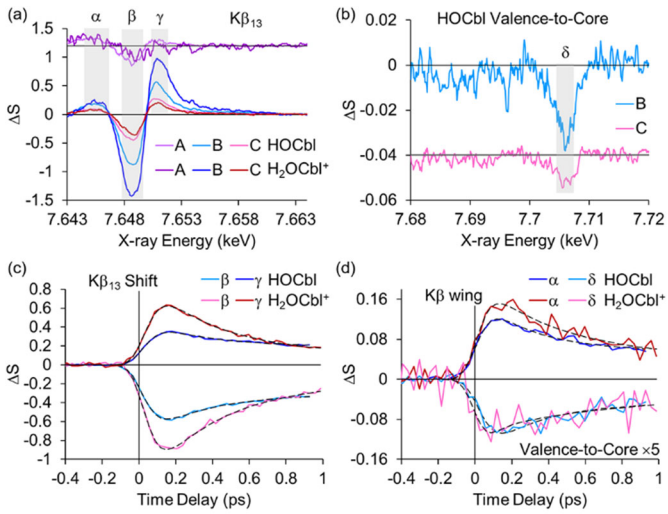

Figure 9. Global analysis of the Co $K\beta_{1,3}$ and valence-to-core emission bands of H_2OCbl^+ and HOCbl following 550 nm excitation. (a) Species associated difference spectra in the $K\beta_{1,3}$ region for the three species **A**, **B**, and **C**. The spectra for **A** are offset for clarity. (b) Species associated difference spectra in the valence-to-core region for species **B** and **C** following excitation of HOCbl. Similar trends are observed for H_2OCbl^+ although the data are much noisier (See Figure S11). (c) The time dependence of the difference signal in the regions of panel (a) designated β and γ. These regions probe the blue shift of the emission band in the excited state. This shift is larger for H_2OCbl^+ than for HOCbl, consistent with the results following 400 nm excitation in Figure 7(c,f). (d) The time dependence of the difference signal in the region of panel (a) designated α and the portion of the valence-to-core spectrum in panel (b) designated δ. The transients in these regions were used to assign the time zero point for maximum overlap of the optical and X-ray pulses.

The results presented above suggest that even the changes at very short times are similar for 400 nm and 550 nm excitation. The initial transient, **A**, is characterized by a small red-shift of the $K\beta_{1,3}$ emission that is evident primarily on the low-energy wing of the emission band. The magnitude of the shift is similar for H_2OCbl^+ and HOCbl. The $\pi\rightarrow\pi^*$ excitation of the corrin ring results in a small expansion around the cobalt and a modest change in the intensities and/or energies of the underlying transitions in the $K\beta_{1,3}$ emission band. The bleach at the peak of the valence-to-core transition also appears at very early times consistent with involvement of the nitrogen atoms in the corrin ring in the $\pi\rightarrow\pi^*$ excitation. A decrease in the emission intensity could result from an increase in the Co-N bond lengths[61] and/or the removal of electron density from the π orbitals.

The evolution to species **B** is accompanied by a significant blue-shift of the $K\beta_{1,3}$ emission, an increase in emission in the region often designated as Kβ′ (see Figure 8(g)), and a decrease in emission in the high energy wing of the valence-to-core transition as illustrated in Figure 10.

Finally, the similarity of the UV-visible spectra, the XANES spectra, the Kβ$_{1,3}$ emission spectra, and the transients in the valence-to-core region for the species designated **C** challenges our earlier hypothesis that these are qualitatively different kinds of states for H_2OCbl^+ and HOCbl.

The valence-to-core emission following excitation of ground state H_2OCbl^+ and HOCbl was simulated as described in Experimental Methods. The single transition at the peak of the of the emission for H_2OCbl^+ involves contributions from cobalt p_x and the p_x and p_y orbitals of the equatorial nitrogen atoms. There is no significant contribution from the axial ligands. The calculation predicts that this transition is polarized along the *x*-axis. In contrast, there are three orbitals contributing to the peak of the emission for HOCbl with all three including contributions from the axial ligands in addition to cobalt p_x and p_y and the p_x and p_y orbitals of the equatorial nitrogen atoms with transitions polarized near the Co-N bonds rather than along the *x*- or *y*-axes. The orbitals corresponding to the two most intense transitions are plotted in Figure 10.

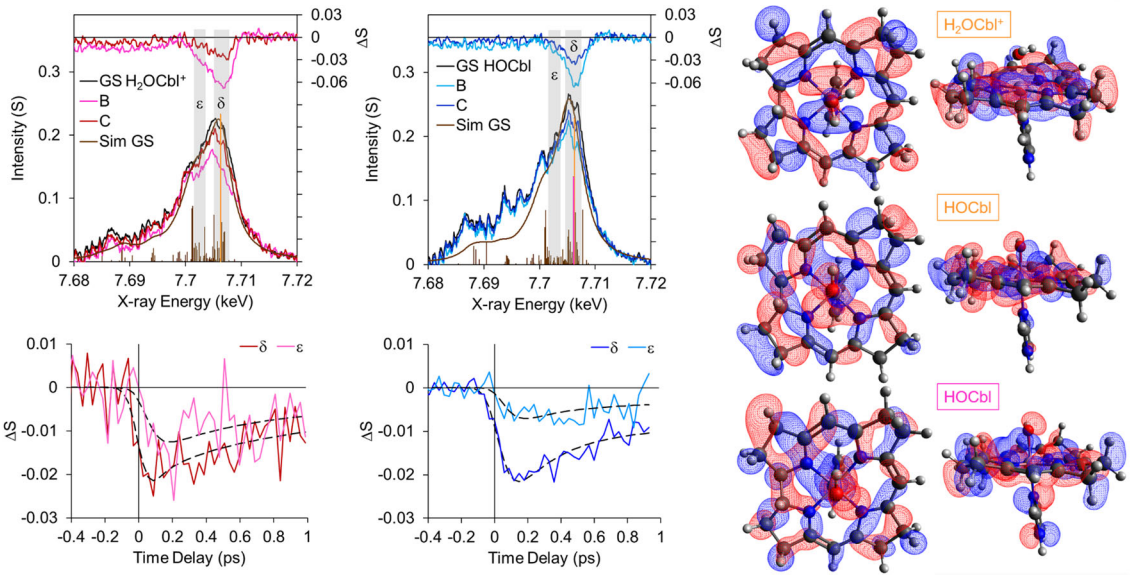

Figure 10. Comparison of the time dependence in the Co valence-to-core region for H_2OCbl^+ and HOCbl. The difference spectra plotted in the upper panel were obtained for a time delay of ca. 200 fs (**B**) and 1 ps (**C**). Calculated emission spectra for the ground state are plotted as stick plots indicating the transitions and broadened using a Lorentzian lineshape with Γ=4.5 eV for comparison

with the experimental results. The time dependence of the signal integrated over the regions labeled δ and ε is plotted in the lower panels. The orbitals plotted to the right represent the dominant contribution at the peak of the H_2OCbl^+ emission (orange stick) and the two largest contributions at the peak of the HOCbl emission (orange and pink sticks).

Polarized UV-Visible Transient Absorption

The polarized UV-visible transient absorption data reported previously[11] are replotted in Figure 11 using the decomposition into directional components as outlined in Eq. 2 for the three species **A** (~30fs), **B** and **C**. These plots make it clear that the transition dipole responsible for the αβ-band (designated *x* in Figure 1) and the transition dipole responsible for the γ-band are approximately orthogonal as shown by fact that their transient bleaches are almost completely *x* and *y*+*z* polarized, respectively. The picosecond excited state spectra **C** for H_2OCbl^+ and HOCbl are very similar in the αβ-band region, while their γ-bands remain distinctive (see also Figure S5). Of more significance for comparison with the X-ray spectra, there is a structured bleach at ca. 400 nm for both molecules that is polarized orthogonal to the *x*-direction (i.e. it shows up in the *y*+*z*-polarized contribution, but not in the *x*-polarized contribution to the total signal). This bleach and its polarization was not obvious in the way the data was presented previously.[11] The two electronic transitions bleached at ca. 390 nm and 412 nm for H_2OCbl^+ are similar to peaks identified in the ground state MCD spectrum reported by Brunold and coworkers and assigned to $\pi\rightarrow\pi^*/3d_{xy}$ transitions.[62]

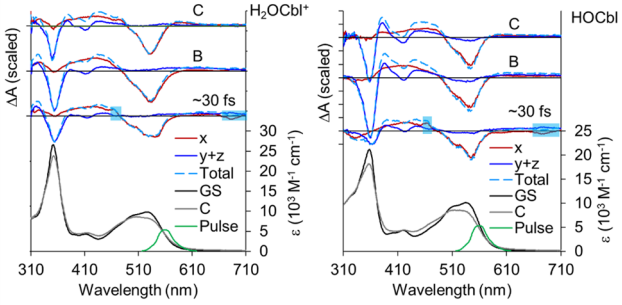

Figure 11. Plots of the polarization decomposition of the difference spectra for the excited states of H_2OCbl^+ (left) and HOCbl (right). The ground and C state absorption spectra of H_2OCbl^+ and HOCbl are also compared in each panel. The excitation pulse spectrum (same for both measurements) is shown for comparison. Similar results are obtained for H_2OCbl^+ with an excitation pulse centered around 530 nm (see Figure S4). The blue boxes on the 30 fs spectra indicate regions where stimulated Raman scattering from the solvent contributes to the signal. The arrows indicate the orthogonally polarized bleaching signal discussed in the text.

XANES Simulations

The Ground States of H_2OCbl^+ and HOCbl. The ground state XANES spectra of both H_2OCbl^+ and HOCbl were simulated using the FDMNES software[63,64] beginning with the crystal structure for H_2OCbl^+ reported by Kratky et al.[65] These are shown, together with the experimental data in Figure 12. Because the XANES spectra of H_2OCbl^+ and HOCbl are similar, we have used the same corrin ring to model both compounds modifying only the axial groups. The crystallographically determined structures show similar axial ligation for H_2OCbl^+ (Co-N_{DMB} 1.925 Å, Co-O 1.952 Å) and HOCbl (Co-N_{DMB} 1.985 Å, Co-O 1.919 Å), although the Co-N_{DMB} distance reported for H_2OCbl^+ (1.925 Å) is significantly shorter than reported for other similar cobalamins.

We find that our simulations of the ground-state spectrum of H_2OCbl^+ give somewhat better agreement if we use axial bonds lengths that are slightly longer than the crystallographic values (Figure 12). However, the simulations are nearly identical for a range of axial bond lengths from (Co-N_{DMB} 2.00 Å, Co-O 1.95 Å) to (Co-N_{DMB} 1.95 Å, Co-O 2.00 Å) (see Figure S12) providing the average axial bond length remains ~1.975 Å. Any of these structures could be used to represent the ground state. In what follows, we will compare the excited state spectra to those for a ground state simulation in which both axial bonds have the same length, (Co-N_{DMB} 1.975 Å, Co-O 1.975

Å), bearing in mind that a range of structures with the sum of the axial bond lengths ca. 3.95 Å are equally plausible. This is also the structure that was used for the ground state XES and pre-edge XAS calculations plotted above (Figures 5 and 10). In contrast to the adjustments needed for H_2OCbl^+, the axial bond lengths reported in the crystal structure for HOCbl[66] result in a simulation that agrees reasonably well with the experimental data. Thus, we have used these bonds lengths for the ground state of HOCbl.

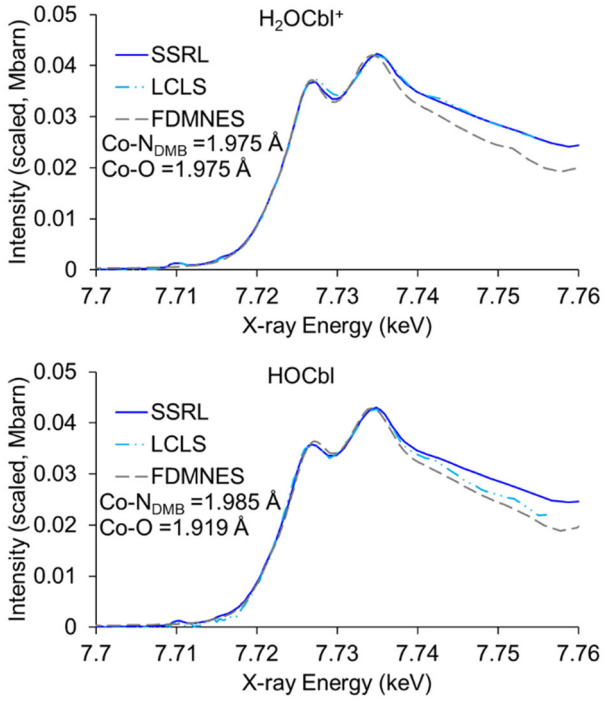

Figure 12. Comparison of the ground state Co XANES spectra of H_2OCbl^+ and HOCbl obtained in room temperature solution at LCLS and measurements obtained on frozen solution samples at SSRL. FDMNES simulations of the ground state are also plotted with axial bond lengths as indicated. The spectra are scaled to the calculated intensity in Mbarns/atom.

The initial excited state A. The XANES spectrum of the initial excited state populated following excitation of H_2OCbl^+ is estimated from the signal at the very earliest times, assuming that the population at t=0 is 50% of the maximum. Excitation of a $\pi \rightarrow \pi^*$ transition of the corrin

ring is expected to expand the cavity around the cobalt due to a general weakening of ring bonds. In order to model this initial state in a chemically reasonable fashion, we start with the hypothesis that the excited state ring will resemble the ring that is seen if a larger metal is substituted for the Co^{3+}. A good candidate is Rh^{3+} and there is a crystal structure of chlororhodibalamin (ClRbl) available that can be used to simulate the structural change upon excitation.[67] The average expansion of the Co-N_{Corrin} bonds in ClRbl relative to the ground state ring of H_2OCbl^+ is 0.077 Å, accompanied by some ruffling and expansion of the outer ring. Substituting the rhodibalamin ring for the cobalamin gives a predicted XANES spectrum that changes relative to the ground state in the same way that **A** changes. This can be seen by comparing the dark blue (experimental) and solid red simulations in Figure 13, confirming the expectation that the fastest motions are in the ring. Although the experimental polarization decomposition for **A** is noisy (Figure 4), it is consistent with the polarized predictions for the rhodibalamin ring (dashed, and dotted red lines, Fig. 13). A somewhat smaller increase in the average axial bond length in **A** (ca. 0.075 Å) leaves the *x* and *y* components of the difference spectrum essentially unchanged while giving an increase in the *z* component and thus in *y*+*z*. This gives a slightly better fit, as shown by the light-blue and magenta lines in Figure 13, but it is not possible distinguish between expansion of the Co-O bond, the Co-N_{DMB} bond, or a combination of these. While it is possible that distortions other than those seen in rhodibalamin might give similarly good results, it is clear from the polarization dependence that the principle qualitative change immediately following excitation is an increase in the size of the cobalamin cavity around the central cobalt atom.

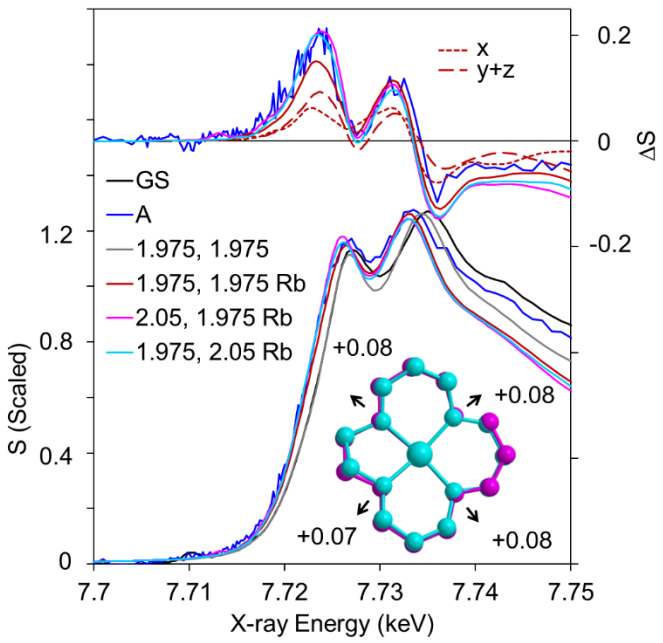

Figure 13. Comparison of the ground (GS) and initial excited state (species **A**) Co XANES spectra of H_2OCbl^+ with FDMNES simulations. The bright blue lines are the experimental excited state difference spectrum and estimated XANES spectrum. The solid black line is the experimental ground state spectrum of H_2OCbl^+. The parameters for the FDMNES simulations are indicated in the legend as Co-N_{DMB}, Co-O bond lengths in Å. Rb designates use of the rhodibalamin ring for the excited state (CCDC 2017112). The expansion of the ring is illustrated in the inset, with light blue atoms representing the ground state structure and magenta atoms the excited state. The dashed lines in the upper plot represent the polarization decomposition for the difference spectra without changes in the axial bonds illustrating that the *x* and *y*+*z* contributions are comparable.

Species B at ca. 150 fs. The difference spectrum for **B** is much larger than for **A** and is polarized primarily in the *y*+*z* direction, indicating that the expansion of the cavity in **A** is followed by a rapid expansion in the *z*-direction by one or both axial bonds. For an excitation fraction of *f*=0.4, the excited state spectrum at this time delay is well modeled using Co-N_{DMB} from 2.6 Å to 2.7 Å and Co-O of 2.10 Å as illustrated in Figure 14. Because the excitation fraction affects our estimate of the absolute magnitude of the difference spectrum, any error in excitation fraction

could, in principle, change this conclusion. Fortunately, the excitation fraction can be constrained to being between 0.4 and 0.5 as discussed in Supporting Information. As shown in Figure S13, an excitation fraction of 0.5 does not substantively change the comparison of simulations with experiment.

Expansion of the Co-O bond instead of the Co-N_{DMB} bond does not agree as well with the measured difference spectrum, as shown on the right hand side of Figure 14. However, the difference in the fits is small and is not sufficient to rule out the long Co-O possibility. Simulations of H_2OCbl^+ for a broad range of bond lengths are plotted in Figure S15. Of particular note, these simulations show that a symmetric expansion of both bonds does not give as good agreement with the measured difference spectrum as do either of the asymmetric expansions. Similar results are obtained for HOCbl as illustrated in Figure 15.

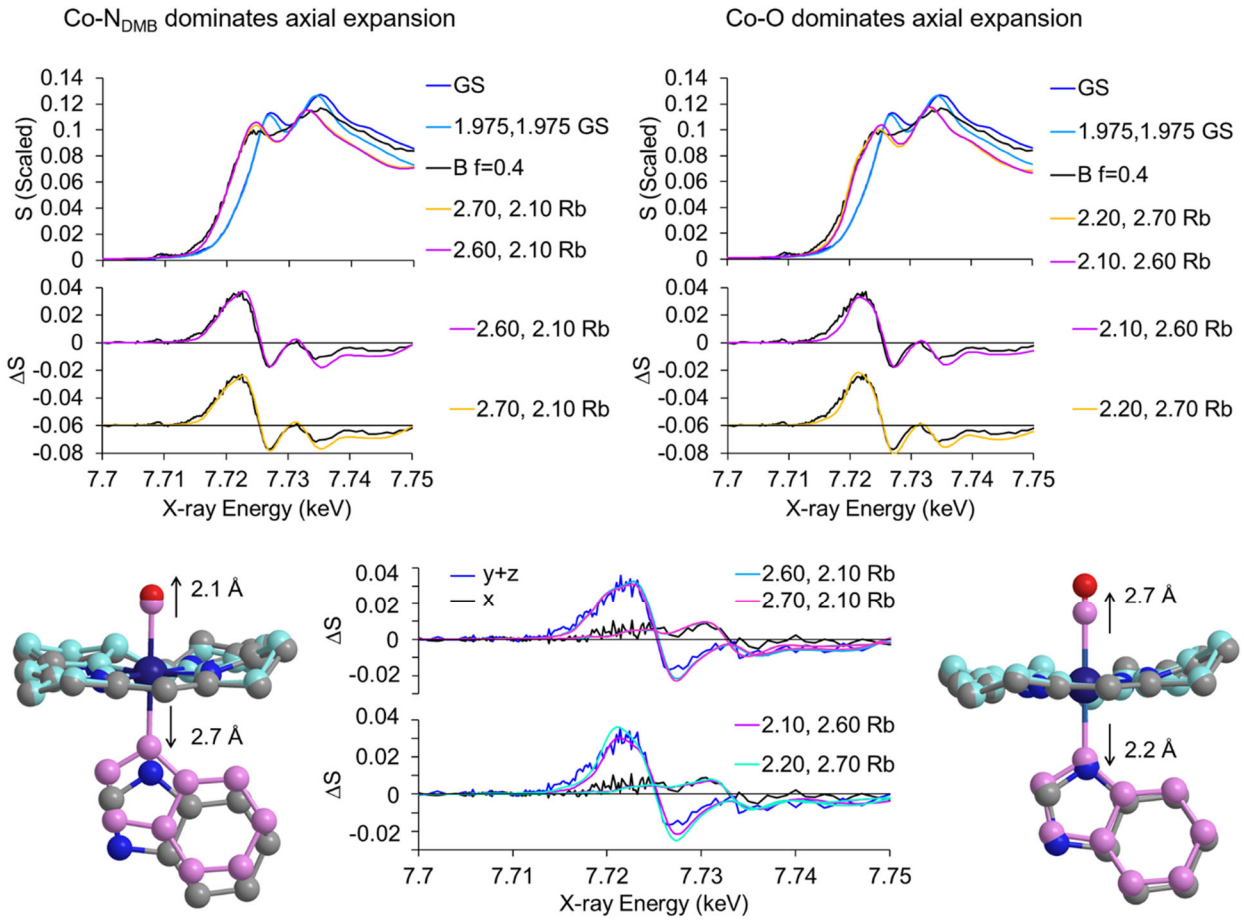

Figure 14. Comparison for H_2OCbl^+ of simulated and experimental Co XANES spectra for the species **B**, present at 150 fs. The axial bond lengths are as indicated (Co-N_{DMB}, Co-O in Å) and the rhodibalamin structure is used to model the ring distortion in the excited state. The lower row of the figure illustrates the magnitudes of the predicted distortions, with the ground state in pastel blue (ring) and pink (axial groups), and the comparison of select simulations with the polarization decomposition of the experimental measurement.

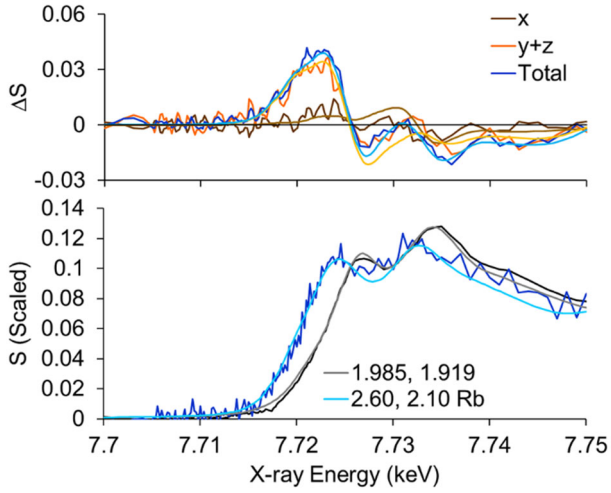

Figure 15. Comparison of the experimental and simulated Co XANES spectra of HOCbl species **B** for the axial bond lengths indicated in the figure (Co-N_{DMB}, Co-O in Å) and the excited state ring approximated with the rhodibalamin ring.

Species C, t>400 fs. The final species preceding ground state recovery exhibits a lifetime of 2.3 ± 0.3 ps for H_2OCbl^+ and 5.3 ± 0.4 ps for HOCbl. The absence of a significant *x*-polarized component in the XANES difference spectrum (Figure 4) and the similarity of the UV-visible ground and excited state spectra (Figure 11 and Figure S5), indicate that for both molecules the corrin ring has recovered to a structure that is similar to the ground state structure. Thus, the FDMNES simulations for **C** used the ground state structure for the corrin ring (See Figure S17). The best agreement was found for an expansion of the Co-N_{DMB} bond to ca. 2.25 Å accompanied by a small contraction of the Co-O bond to ca. 1.88 Å. As illustrated in Figure 16, this model does an excellent job of reproducing both the large *y*+*z* component and the small x component of the difference spectra. The opposite change, with contraction of the Co-N_{DMB} bond and expansion of the Co-O bond, does not agree with the data, overestimating the size of the bleach at 7.726 keV (See Figure S17e).

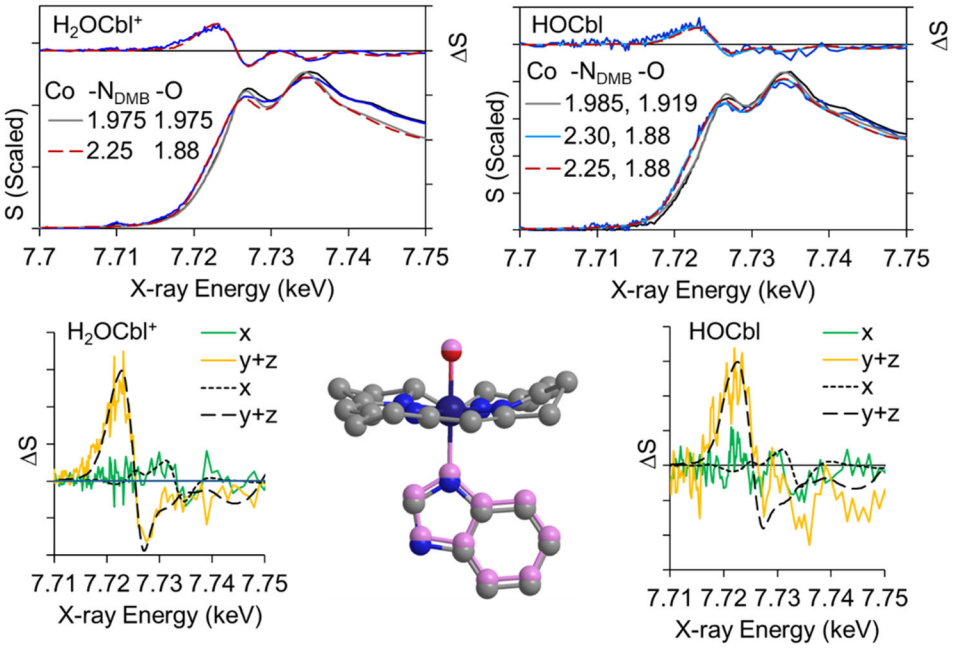

Figure 16. The upper plots compare the experimental (dark blue lines) and simulated Co XANES spectra of species **C** in H_2OCbl^+ and HOCbl for the axial bond lengths indicated in the figure. The ground state spectra are also shown (black lines). The lower plots compare the experimental and simulated decomposition into *x* and *y+z* components. The structure (lower middle) illustrates the magnitudes of the predicted distortions for state **C** with the ground state in pink for the axial groups.

DISCUSSION

The combination of transient optical and X-ray spectroscopy provides detailed picture of the excited state dynamics and subsequent relaxation of H_2OCbl^+ and HOCbl. The initial excitation into the visible absorption band results in prompt expansion of the bonds around the central cobalt atom. The magnitude of the change is consistent with population of a ππ* excited state followed by ligand to metal charge transfer populating a $\pi\sigma^*(3d_{z^2})$ state. The crystal structure for ClRbl provides a good model for the corrin ring in this excited state because the radius of the six-coordinate 4d transition metal Rh^{3+} ion is expected to be approximately the same as that of six-coordinate Co^{2+}. The X-ray emission spectrum in the $K\beta_{1,3}$ region is characterized by a small

increase in the low energy wing around 7.645 keV and a prompt decrease of the valence-to-core emission centered at 7.707 keV. The change in the $K\beta_{1,3}$ region is distinct from the changes observed at later times (species **B** and **C**, below) and consistent with a small shift to lower energy (~0.1 eV). In **A**, it may be that the π-π^* excitation moves electron density from the corrin nitrogens to the ring π^* orbitals, decreasing the ability of the corrin to shield the Co 3p orbitals and thus lowering very slightly the Kβ emission energy.

The species **A** is followed by ligand to metal charge transfer populating a $\pi\sigma^*(3d_{z^2})$ state in which the Co is, at least formally, reduced to Co^{2+}. Population of the metal-ligand antibonding $\pi\sigma^*(3d_{z^2})$ state is followed by rapid expansion of the axial bonds. Earlier TDDFT simulations gave predicted excited state potential energy surfaces for HOCbl and H_2OCbl^+.[11] From these, one can predict that the outer turning points – that is, the points that have an energy consistent with an inner turning point at the ground state axial bond lengths – will occur around Co-N_{DMB} 2.6 Å, Co-O 2.15 Å for H_2OCbl^+ and Co-N_{DMB} 2.6 Å, Co-O 2.1 Å for HOCbl. We attribute the species **B** (i.e., the structure observed at ca. 150 fs) to the outer turning point of the excited state potential energy surface. The excited state dynamics are best described as ballistic motion on the excited state potential energy surface with the XANES difference spectra dominated by the turning points. Although the kinetic behavior can be fit using a sequential exponential model, the displacements, which are what drives the XANES changes, are unlikely to be well modelled using exponential kinetics.

The XANES spectra for H_2OCbl^+ and HOCbl are similar at the point of maximum displacement (species **B** above), although the predicted axial bond elongation may be slightly larger for $H_2OCbl^{+\cdot}$ In contrast to the XANES similarity, the UV-visible spectra (Figure S5) and the X-ray emission spectra (Figures 7-10) all exhibit distinct differences. In particular, the larger

blue-shift in the $K\beta_{1,3}$ emission band of H_2OCbl^+, along with the larger change in the region often designated as $K\beta'$ and the stronger bleach in the valence-to-core emission, reflect differences in the electron density around the central cobalt atom for these two molecules.

The up-down-up pattern seen in the $K\beta_{1,3}$ emission difference signal for **B** has been attributed previously to changes in the metal spin state.[68-70] Spin-spin coupling between unpaired spin in the d-orbitals and in the $3p^5$ shell causes a change in the splitting of the Kβ multiplets giving rise to this more complex difference pattern. For example, the difference between the Kβ emission for the low-spin Fe(II) complexes FeS_2 and $K_4Fe(CN)_6$ is very similar to that seen for **B** vs. the cobalamin ground state. Low-spin Fe(II), like the low-spin Co(III) in cobalamins, has S=0 and thus should not, to a first approximation, have any spin-exchange. For Fe(II), the observed differences were attributed to configuration interaction mixing of d^6 Fe(II)L + d^7 Fe(I)(L^+). By analogy, we attribute the difference signal in **B** to formation of an electronic state with significant d^7 Co(II)(L^+) character. An estimate of the effective change in spin (ΔS) can be obtained using the calibrated spin values estimated by Lafuerza et al.[68] adjusted for the increase in Slater exchange integrals for Co vs. Fe.[69] The Integrated Absolute Difference (IAD)[68] for **B** relative to the ground state suggests ΔS values of ~0.5 and ~0.3 for H_2OCbl^+ and HOCbl respectively. This would be consistent with a low-spin Co(II), as is typical for Co(II)alamin.

The rebound of the axial bonds leads to formation of a species **C** with a picosecond lifetime for both H_2OCbl^+ and HOCbl. These states have strikingly similar spectroscopic properties, including similar persistent decreases in valence-to-core emission intensity, similar molecular structures as deduced from XANES, similar Kβ mainline differences, and similar bleaches of the transitions around 410 nm in the UV-visible absorption spectra. The FDMNES simulations of **C** suggest that the corrin ring around the cobalt ion has recovered to a structure similar to the ground

electronic state, while the Co-N_{DMB} bond is longer than in the ground state (Δr ca. 0.25 Å to 0.35 Å) and the Co-O bond is shorter than in the ground state (Δr ca. -0.04 to -0.1 Å). Together, these observations all lead to the hypothesis that the state **C** for both H_2OCbl^+ and HOCbl is a metal-centered excited state with modifications in the 3d electronic distribution accounting for the differences in the absorption and emission spectra relative to those for **B**.

The difference signal in the $K\beta_{1,3}$ emission for **C** has the same shape as **B**, but lower amplitude reflecting a smaller amplitude in the blue-shift of the mainline emission (see Figure 7(e) and (f)). The decrease in difference amplitude is consistent with increased covalency as the axial and equatorial bond lengths contract and the evolution of the electronic structure to a metal-centered d^6 Co(III) excited state. The IAD values for **C** suggest an effective ΔS of ~ 0.2 relative to the ground state.

While the cobalt contribution to the most intense valence-to-core emission transition is primarily $p_x \rightarrow 1s$, the other transitions in the region designated δ in Figure 10 have significant contributions from d_{xz}, d_{yz}, and $d_{x^2-y^2} \rightarrow 1s$. A decrease in the electron density in these 3d orbitals or a change in the mixing with Co p_x or p_y orbitals could account for the persistent decrease in emission intensity around 7.707 keV. This decrease does not appear to be related to the changes in axial bond lengths (see SI and Figure S18). The preservation of intensity in the $1s \rightarrow \sigma^* 3d_{z^2}$ pre-edge transition in the XAS and the bleach of transitions assigned to $\pi \rightarrow \pi^*/3d_{xy}$ around 410 nm in the optical spectrum[62] suggests that electron density may have moved from $3d_{z^2}$ to $3d_{xy}$, although it also possible that a change in the relative energies of the $3d_{z^2}$ and $3d_{xy}$ orbitals changes the $\pi \rightarrow \pi^*/3d_{xy}$ transition and increases the mixing of $3d_{z^2}$ with Co $4p_z$. A simplified schematic of this evolution is shown in Figure 17.

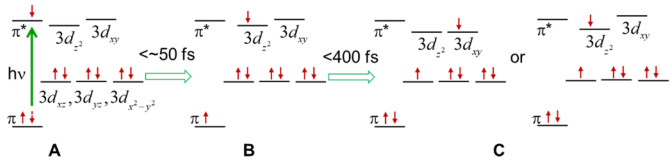

Figure 17. Simplified 1-electron schematic illustration of the evolution of electron density following photoexcitation of H_2OCbl^+ and HOCbl. Calculated molecular orbitals of cobalamins are mixtures of ligand and cobalt orbitals and changes in the relative contributions may account for the observations.

The evolution of electron density outlined in Figure 17 is also consistent with the time-dynamics of the emission in the region often designated as Kβ′ illustrated in Figure 7(g) and Figure 18. An increase in emission intensity, consistent with an increase in spin-density at the cobalt, is observed as the excited state evolves into a $\pi^1\left(\sigma^*3d_{z^2}\right)^1$ configuration. The increase is larger for H_2OCbl^+ than HOCbl, perhaps reflecting the somewhat longer apparent axial distances in the former. The emission in this region decreases as the electronic configuration evolves into a metal-centered excited state, but remains higher than the ground state for the duration of the excited state lifetime (see Figure 8(g) State **C** and Figure 18).

Both of the configurations suggested for **C** in Fig. 17 are low-spin, S=0. This is consistent both with the lack of any evidence for intersystem crossing in these cobalamins and with the very small IAD, which is inconsistent with a high-spin Co(III). The fact that the apparent ΔS (~0.2) is small but not zero for **C** suggests differences in the importance of configuration interaction mixing for the latter.

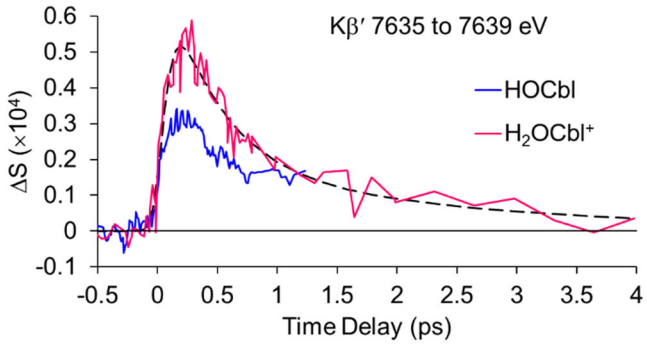

Figure 18. Time dependent evolution of the X-ray emission in the Co Kβ′ region following excitation of H_2OCbl^+ and HOCbl at 400 nm. The difference signal is integrated over the energy range indicated. The dashed black line is the fit to this region obtained from a global analysis of the XES data for H_2OCbl^+. The longest decay constant is 2.4 ps.

The difference in the time-constants and relaxation dynamics for HOCbl and H_2OCbl^+ reflect quantitative rather than qualitative differences between these two molecules. The barrier for internal conversion back to the ground state is larger for HOCbl than for H_2OCbl^+ accounting for the longer excited state lifetime. In addition, the prominent relaxation component in the UV-visible TA spectrum of H_2OCbl^+ compared with HOCbl (see Fig. 6 of ref.[11]) suggests that the metal-centered state is lower in energy for H_2OCbl^+ than HOCbl allowing the dissipation of vibrational energy while in the electronic excited state to play a more prominent role in the observed transient signals.

CONCLUSIONS

The combination of tr-XAS in the pre-edge and XANES regions, $K\beta_{1,3}$ and valence-to-core tr-XES, and transient UV-visible spectroscopy, provides a powerful tool to probe the femtosecond and picosecond electronic and structural dynamics photoactive transition metal complexes. Here we have focused on the detail available using these methods to probe the dynamics of photo-excited HOCbl and H_2OCbl^+. The measurements and simulations reported here demonstrate that

both molecules follow similar excited state pathways, contrary to prior hypotheses based on UV-visible spectroscopy and quantum chemical calculations.[11] Polarized XANES difference spectra allow identification of sequential structural evolution involving the equatorial and axial ligands. Time-resolved XES, especially in the valence-to-core region, along with polarized optical transient absorption leads to the hypothesis that both molecules form a metal-centered excited state with a lifetime of 2 to 5 picoseconds. More detailed simulations of the XES and the XAS pre-edge transition as well as time-resolved X-ray measurements at the Co L-edge and N K-edges will provide more detailed insight into the electronic evolution in the excited state. These measurements will be enabled by upcoming developments at both LCLS and the EuXFEL.

EXPERIMENTAL METHODS

XANES Measurements. XANES difference spectra, $\Delta S(t) = S_{on}(t) - S_{off}$, were obtained for time delays between -0.5 ps and 2 ps using the XPP instrument of the X-ray free electron laser LCLS at SLAC.[71] Hydroxocobalamin hydrochloride sample was dissolved in ultrapure deionized water buffered at pH 5 (H_2OCbl^+) or pH 10 (HOCbl) and pumped through a fused silica nozzle to achieve a stable 50 μm diameter jet of recirculating solution. The X-ray beam and laser beam travel in a nearly collinear geometry (~1° crossing angle) and were overlapped with the sample about 500 μm from the nozzle. The optical pump pulse (~50 fs full width at half maximum (FWHM)) was centered at 520 nm. The X-ray probe pulse (~40 fs FWHM) was tuned from 7.7 keV to 7.76 keV by using a Si(111) channel cut monochromator (1.4×10^{-4} ΔE/E resolution) and cobalt X-ray fluorescence was collected and used as a measure of X-ray absorption where the signal was normalized to the X-ray scattering from the solvent. More details are found elsewhere.[21,22,33] The jitter between the X-ray and optical laser was recorded pulse by pulse and used to sort the XANES

spectra into finer time steps. The data were averaged using 50 fs bins centered every 25 fs.

Time-resolved XANES measurements were performed on H_2OCbl^+ buffered at pH 5 during two different runs at XPP. The first used a sample concentration of 5 mM, covered the time range from -0.4 ps to 1.2 ps, and achieved an excitation fraction of ca. 0.25, similar to the fraction determined for MeCbl during the same run as described previously.[72] During the second run, excellent data were obtained for a 12 mM sample buffered at pH 5, with a nominal pulse energy of 5 μJ/pulse covering the time range from -0.4 ps to 2 ps. We estimate an excitation fraction of approximately 0.4 for these spectra (see SI for additional details).

The combined final instrument response function, including the X-ray and optical laser pulse durations, was determined by fitting the pre-edge region of propylcobalamin data measured immediately after the H_2OCbl^+ measurement. The pre-edge bleach of propylcobalamin, like the pre-edge bleach of AdoCbl, is strong and provides an upper limit for the intrinsic time resolution of the measurement.[21] The fit yielded a Gaussian with a full width at half maximum (FWHM) of 112 fs (σ = 47.8 fs). The time zero point for maximum overlap of the optical and X-ray pulses was assigned by using the earliest XANES difference signals for H_2OCbl^+ observed at 7.708 keV and 7.731 keV as well as the *x*-polarized component at 7.723 keV (see Figure S1).

During the second run, measurements were also performed for 12 mM HOCbl buffered at pH 10. A high potassium concentration (~1 M instead of 10 mM) complicated the measurement by adding background scatter to the signal. Four time-resolved XANES scans for the HOCbl sample, two for each polarization, were obtained at a relatively high optical pulse energy (nominally 6 μJ/pulse, estimated excitation fraction 0.5) covering the time range from -0.4 ps to 2 ps. An additional 10 scans, five for each polarization, were obtained at a lower optical pulse energy (nominally 4 μJ/pulse, estimated excitation fraction 0.25) covering the time range from 0.1 ps to

2 ps. To ensure that the higher ionic strength did not perturb the excited state dynamics, optical transient absorption measurements were performed for 1 M and 10 mM buffers with identical results (see Figure S3).

For all XANES measurements, the polarization of the optical pulse was rotated using a remote-controlled optical waveplate to be oriented either perpendicular or parallel to the polarization of the X-ray pulse. The difference signal with each polarization can be used to obtain the component parallel to the excited transition dipole moment and the sum of the components perpendicular (see Eq. 2). Because the ground state molecules are randomly oriented in solution, as the excitation fraction approaches or exceeds 1/3 the polarization discrimination introduced by the excitation pulse must decrease. If the excitation fraction is 1, all molecules in the sample are excited and no polarization discrimination remains. The polarization discrimination for the first run (excitation fraction ca. 0.25) is good, but the higher excitation fraction for H_2OCbl^+ during the second run resulted in a slight decrease in polarization discrimination. The latter data were corrected as described in supporting information and validated by comparison with the results from the first run (see Figure S9). For HOCbl, polarization analysis was only performed for the lower excitation fraction (ca. 0.25).

XANES spectra of ground state H_2OCbl^+ and HOCbl were also obtained at SSRL beamline 9-3 for comparison with the LCLS measurements and for better intensity scaling of the simulated and experimental spectra. Hydroxocobalamin hydrochloride was dissolved in 50 mM phosphate (pH 5) or carbonate (pH 10) buffer and frozen. Data were collected using a Si(220) monochromator, and a Rh-coated mirror with an energy cutoff of 9 keV used for harmonic rejection. The samples were measured at 10 K using a He-cooled cryostat in fluorescence mode and a 100-element Ge detector array equipped with Soller slits and an Fe filter. Four successive

spectra (each ~ 5 minutes of data acquisition) were compared to ensure that there was no X-ray induced radiation damage. Data were normalized using M-Back.[73]

XES Measurements. XES difference spectra for HOCbl and H_2OCbl^+ in the Co $K\beta_{1,3}$ and valence-to-core regions were obtained at the FXE instrument of the European X-ray free electron laser (EuXFEL).[74-76] The incident X-ray energy was 9.3 keV. Emission spectra were measured with a dispersive X-ray spectrometer operating in the von Hamos geometry and equipped with 7 Ge(111) analyzers at ~83 degrees for measuring Co Kβ. All cylindrical analyzers have 500 mm radius of curvature. The Co Kβ signal was recorded using a Jungfrau 500K detector. The detector integrated all pulses (total 75 or 150) in a train at 10 Hz. The pump-probe signal was generated by pumping every second train (5 Hz) and the differences are constructed by subtracting one train ON minus one train OFF after normalization to the total integrated Kβ intensity. The sample was delivered as a 100 μm thick cylindrical jet running with a linear speed of 60 m/s.

Two sets of XES measurements were performed. The first set used an excitation wavelength 400 nm, 70 fs duration (FWHM), and a laser/X-ray crossing angle of ca. 15°. To avoid distortions due to detector gain switching, the image from each XFEL pulse train was examined, and pixels where the intensity caused a switch to lower gain were omitted from the average. An approximate time zero was determined by fitting a Gaussian-broadened Heaviside step function to the maximum in the Kβ transient. Because the rises of these signals are delayed, the time zero point for maximum overlap of the optical and X-ray pulses was refined by using the earliest transient signals, particularly the signal observed around 7645.5 eV (See Figure S2). The second set of measurements were performed with an excitation wavelength 550 nm, 70 fs duration (FWHM), and a laser/X-ray crossing angle of ca. 2°. The spectrometer and detector were aligned to capture the valence-to-core region for these measurements. The earliest transient signals in these

measurements were observed in the valence-to-core region and these were used to assign the time zero point for maximum overlap of the optical and X-ray pulses (see below). The IAD was calculated as described in Ref. [68].

UV-Visible Transient Absorption. UV-visible TA spectra of HOCbl, and H_2OCbl^+ were obtained as reported previously.[11,42] New measurements were performed to characterize the polarized response following excitation at 400 nm and to test the influence of ionic strength on the transient absorption signal for HOCbl (Figure S3).

Computational Methods. The Finite Difference Method Near Edge Structure (FDMNES) program was used to simulate the ground and excited state XANES spectra as a function of molecular structure.[63,64] XES spectra in the valence-to-core region were simulated using Orca 4.2.1[57] to perform density functional theory (DFT) calculations with the B3LYP functional and ZORA-def2-TZVP basis. The pre-edge XAS spectrum was simulated using Orca 4.2.1 to perform time-dependent density functional theory (TDDFT) calculations with the B3LYP functional and ZORA-def2-TZVP basis.

SUPPORTING INFORMATION

Details of the beamtime proposals and data recorded for the experiment at the European XFEL are available at doi:10.22003/XFEL.EU-DATA-002715-00 and doi:10.22003/XFEL.EU-DATA-003079-00.

A pdf file including details of data analysis and modeling along with additional figures of experimental data and of FDMNES simulations as a function of structural parameters is available.

ACKNOWLEDGEMENTS

This work was supported by grants from the National Science Foundation NSF-CHE

1836435, NSF-CHE 2154157 to RJS. PAD was supported by an REU award (NSF-PHY 1757574). Use of the Linac Coherent Light Source (LCLS), SLAC National Accelerator Laboratory, is supported by the U.S. Department of Energy, Office of Science, Office of Basic Energy Sciences under Contract No. DE-AC02-76SF00515. Use of the Stanford Synchrotron Radiation Lightsource, SLAC National Accelerator Laboratory, is supported by the U.S. Department of Energy, Office of Science, Office of Basic Energy Sciences under Contract No. DE-AC02-76SF00515. We would like to thank the staff for their assistance. We acknowledge European XFEL in Schenefeld, Germany, for provision of X-ray free-electron laser beamtime at Scientific Instrument FXE (Femtosecond X-Ray Experiments) and would like to thank the staff for their assistance.

REFERENCES

(1) Rury, A. S.; Wiley, T. E.; Sension, R. J.,Energy cascades, excited state dynamics, and photochemistry in cob(III)alamins and ferric porphyrins. *Acc. Chem. Res.* **2015**, *48*, 860-867, 10.1021/ar5004016.

(2) Pucci, C.; Martinelli, C.; Degl'Innocenti, A.; Desii, A.; De Pasquale, D.; Ciofani, G.,Light-Activated Biomedical Applications of Chlorophyll Derivatives. *Macromol. Biosci.* **2021**, *21*, 2100181, 10.1002/mabi.202100181.

(3) Tebo, A.; Herrero, C.; Aukauloo, A., Porphyrins and Metalloporphrins as Components in Artificial Photosynthesis Research In *Handbook of Porphyrin Science*; World Scientific Publishing Company: 2012; Vol. Volume 34, p 195-237, 10.1142/9789814417297_0016

(4) Galloni, P.; Vecchi, A.; Coletti, A.; Gatto, E.; Floris, B.; Conte, V., Porphyrins as Active Components for Electrochemical and Photoelectrochemical Devices In *Handbook of Porphyrin Science*; World Scientific Publishing Company: 2012; Vol. Volume 33, p 225-415, 10.1142/9789814417297_0011

(5) Hughes, J. A.; Hardman, S. J. O.; Lukinović, V.; Woodward, J. R.; Jones, A. R., Investigating radical pair reaction dynamics of B12 coenzymes 1: Transient absorption spectroscopy and magnetic field effects In *Methods in Enzymology*; Marsh, E. N. G., Ed.; Academic Press: 2022; Vol. 669, p 261-281, 10.1016/bs.mie.2021.12.019

(6) Lukinović, V.; Woodward, J. R.; Marrafa, T. C.; Shanmugam, M.; Heyes, D. J.; Hardman, S. J. O.; Scrutton, N. S.; Hay, S.; Fielding, A. J.; Jones, A. R.,Photochemical Spin Dynamics of the Vitamin B12 Derivative, Methylcobalamin. *J. Phys. Chem. B* **2019**, *123*, 4663-4672, 10.1021/acs.jpcb.9b01969.

(7) Jones, A. R.,The photochemistry and photobiology of vitamin B_{12}. *Photochem. Photobiol. Sci.*

2017, *16*, 820-834, 10.1039/c7pp00054e.

(8) Welfare, J. G.; Mortelliti, M. J.; McGlade, C. A.; Hartman, T. W.; Dempsey, J. L.; Lawrence, D. S.,Assessment of Photoreleasable Linkers and Light-Capturing Antennas on a Photoresponsive Cobalamin Scaffold. *J. Org. Chem.* **2022**, *87*, 5076-5084, 10.1021/acs.joc.1c02931.

(9) Shell, T. A.; Lawrence, D. S.,Vitamin B_{12}: A tunable, long wavelength, light-responsive platform for launching therapeutic agents. *Acc. Chem. Res.* **2015**, *48*, 2866-2874, 10.1021/acs.accounts.5b00331.

(10) Sension, R. J.; Chung, T.; Dewan, P.; McClain, T. P.; Lamb, R. M.; Penner-Hahn, J. E., Time-resolved spectroscopy: Advances in understanding the electronic structure and dynamics of cobalamins In *Methods in Enzymology: Coenzyme B_{12} Enzymes Part B*; Marsh, E. N. G., Ed.; Academic Press: 2022, p 303-331, 10.1016/bs.mie.2022.01.010

(11) Wiley, T. E.; Miller, N. A.; Miller, W. R.; Sofferman, D. L.; Lodowski, P.; Toda, M. J.; Jaworska, M.; Kozlowski, P. M.; Sension, R. J.,Off to the races: Comparison of excited state dynamics in vitamin B_{12} derivatives hydroxocobalamin and aquocobalamin. *J. Phys. Chem. A* **2018**, *122*, 6693-6703, 10.1021/acs.jpca.8b06103.

(12) Rury, A. S.; Sension, R. J.,Broadband ultrafast transient absorption of iron (III) tetraphenylporphyrin chloride in the condensed phase. *Chem. Phys.* **2013**, *422*, 220-228, 10.1016/j.chemphys.2013.01.025.

(13) Bacellar, C.; Kinschel, D.; Mancini, G. F.; Ingle, R. A.; Rouxel, J.; Cannelli, O.; Cirelli, C.; Knopp, G.; Szlachetko, J.; Lima, F. A.; Menzi, S.; Pamfilidis, G.; Kubicek, K.; Khakhulin, D.; Gawelda, W.; Rodriguez-Fernandez, A.; Biednov, M.; Bressler, C.; Arrell, C. A.; Johnson, P. J. M.; Milne, C.; Chergui, M.,Spin cascade and doming in Ferric Haems: Femtosecond X-ray Absorption and X-ray Emission Studies. *Proc. Natl. Acad. Sci. U.S.A.* **2020**, *117*, 21914-21920,

10.1073/pnas.2004490117.

(14) Consani, C.; Aubock, G.; Bram, O.; van Mourik, F.; Chergui, M.,A cascade through spin states in the ultrafast haem relaxation of met-myoglobin. *J. Chem. Phys.* **2014**, *140*, 025103 025103

10.1063/1.4861467.

(15) Sension, R. J.,Visualizing ultrafast chemical dynamics with X-rays. *Proc. Natl. Acad. Sci. U.S.A.* **2020**, *117*, 26550-26552, 10.1073/pnas.2017806117.

(16) Gaffney, K. J.,Capturing photochemical and photophysical transformations in iron complexes with ultrafast X-ray spectroscopy and scattering. *Chem. Sci.* **2021**, *12*, 8010-8025, 10.1039/D1SC01864G.

(17) Shelby, M. L.; Wildman, A.; Hayes, D.; Mara, M. W.; Lestrange, P. J.; Cammarata, M.; Balducci, L.; Artamonov, M.; Lemke, H. T.; Zhu, D.; Seideman, T.; Hoffman, B. M.; Li, X.; Chen, L. X.,Interplays of electron and nuclear motions along CO dissociation trajectory in myoglobin revealed by ultrafast X-rays and quantum dynamics calculations. *Proc. Natl. Acad. Sci. U.S.A.* **2021**, *118*, e2018966118, 10.1073/pnas.2018966118.

(18) Mara, M. W.; Phelan, B. T.; Xie, Z.-L.; Kim, T. W.; Hsu, D. J.; Liu, X.; Valentine, A. J. S.; Kim, P.; Li, X.; Adachi, S.-i.; Katayama, T.; Mulfort, K. L.; Chen, L. X.,Unveiling ultrafast dynamics in bridged bimetallic complexes using optical and X-ray transient absorption spectroscopies. *Chem. Sci.* **2022**, *13*, 1715-1724, 10.1039/D1SC05034F.

(19) Bergmann, U.; Kern, J.; Schoenlein, R. W.; Wernet, P.; Yachandra, V. K.; Yano, J.,Using X-ray free-electron lasers for spectroscopy of molecular catalysts and metalloenzymes. *Nat. Rev. Phys.* **2021**, *3*, 264-282, 10.1038/s42254-021-00289-3.

(20) Wernet, P.,Chemical interactions and dynamics with femtosecond X-ray spectroscopy and

the role of X-ray free-electron lasers. *Phil. Trans. R. Soc. A.* **2019**, *377*, 20170464, 10.1098/rsta.2017.0464.

(21) Miller, N. A.; Michocki, L. B.; Konar, A.; Alonso-Mori, R.; Deb, A.; Glownia, J. M.; Sofferman, D. L.; Song, S.; Kozlowski, P. M.; Kubarych, K. J.; Penner-Hahn, J. E.; Sension, R. J.,Ultrafast XANES monitors sequential structural evolution in photoexcited coenzyme B_{12}. *J. Phys. Chem. B* **2020**, *124*, 199-209, 10.1021/acs.jpcb.9b09286.

(22) Miller, N. A.; Deb, A.; Alonso-Mori, R.; Glownia, J. M.; Kiefer, L. M.; Konar, A.; Michocki, L. B.; Sikorski, M.; Sofferman, D. L.; Song, S.; Toda, M. J.; Wiley, T. E.; Zhu, D. L.; Kozlowski, P. M.; Kubarych, K. J.; Penner-Hahn, J. E.; Sension, R. J.,Ultrafast X-ray absorption near edge structure reveals ballistic excited state structural dynamics. *J. Phys. Chem. A* **2018**, *122*, 4963-4971, 10.1021/acs.jpca.8b04223.

(23) Miller, N. A.; Deb, A.; Alonso-Mori, R.; Garabato, B. D.; Glownia, J. M.; Kiefer, L. M.; Koralek, J.; Sikorski, M.; Spears, K. G.; Wiley, T. E.; Zhu, D.; Kozlowski, P. M.; Kubarych, K. J.; Penner-Hahn, J. E.; Sension, R. J.,Polarized XANES monitors femtosecond structural evolution of photoexcited vitamin B_{12}. *J. Am. Chem. Soc.* **2017**, *139*, 1894-1899, 10.1021/jacs.6b11295

(24) Gherasim, C.; Lofgren, M.; Banerjee, R.,Navigating the B-12 Road: Assimilation, Delivery, and Disorders of Cobalamin. *J. Biol. Chem.* **2013**, *288*, 13186-13193, 10.1074/jbc.R113.458810.

(25) Banerjee, R.; Ragsdale, S. W.,The many faces of vitamin B_{12}: Catalysis by cobalamin-dependent enzymes. *Annu. Rev. Biochem.* **2003**, *72*, 209-247, 10.1146/annurev.biochem.72.121801.161828.

(26) Toda, M. J.; Mamun, A. A.; Lodowski, P.; Kozlowski, P. M.,Why is CarH photolytically active in comparison to other B12-dependent enzymes? *J. Photochem. Photobiol. B, Biol.* **2020**, *209*, 111919, 10.1016/j.jphotobiol.2020.111919.

(27) Toda, M. J.; Lodowski, P.; Al Mamun, A.; Jaworska, M.; Kozlowski, P. M.,Photolytic properties of the biologically active forms of vitamin B_{12}. *Coord. Chem. Rev.* **2019**, *385*, 20-43, 10.1016/j.ccr.2018.12.017.

(28) Kozlowski, P. M.; Garabato, B. D.; Lodowski, P.; Jaworska, M.,Photolytic properties of cobalamins: A theoretical perspective. *Dalton Trans.* **2016**, *45*, 4457-4470, 10.1039/C5DT04286K.

(29) Sension, R. J.; Harris, D. A.; Stickrath, A.; Cole, A. G.; Fox, C. C.; Marsh, E. N. G.,Time-resolved measurements of the photolysis and recombination of adenosylcobalamin bound to glutamate mutase. *J. Phys. Chem. B* **2005**, *109*, 18146-18152, 10.1021/jp052492d.

(30) Sension, R. J.; Harris, D. A.; Cole, A. G.,Time-resolved spectroscopic studies of B_{12} coenzymes: A comparison of the influence of solvent on the primary photolysis mechanism and geminate recombination of methyl-, ethyl-, n-propyl-, and 5'-deoxyadenosylcobalamin. *J. Phys. Chem. B* **2005**, *109*, 21954-21962, 10.1021/jp053202w.

(31) Sension, R. J.; Cole, A. G.; Harris, A. D.; Fox, C. C.; Woodbury, N. W.; Lin, S.; Marsh, E. N. G.,Photolysis and recombination of adenosylcobalamin bound to glutamate mutase. *J. Am. Chem. Soc.* **2004**, *126*, 1598-1599, 10.1021/ja0396910.

(32) Cole, A. G.; Yoder, L. M.; Shiang, J. J.; Anderson, N. A.; Walker II, L. A.; Banaszak Holl, M. M.; Sension, R. J.,Time-resolved spectroscopic studies of B_{12} coenzymes: A comparison of the primary photolysis mechanism in methyl-, ethyl-, n-propyl-, and 5'-deoxyadenosylcobalamin. *J. Am. Chem. Soc.* **2002**, *124*, 434-441, 10.1021/ja011628s.

(33) Miller, N. A.; Kaneshiro, A. K.; Konar, A.; Alonso-Mori, R.; Britz, A.; Deb, A.; Glownia, J. M.; Koralek, J. D.; Mallik, L.; Meadows, J. H.; Michocki, L. B.; van Driel, T. B.; Koutmos, M.; Padmanabhan, S.; Elías-Arnanz, M.; Kubarych, K. J.; Marsh, E. N. G.; Penner-Hahn, J. E.;

Sension, R. J.,The Photoactive Excited State of the B12-Based Photoreceptor CarH. *J. Phys. Chem. B* **2020**, *124*, 10732−10738, 10.1021/acs.jpcb.0c09428.

(34) Padmanabhan, S.; Perez-Castano, R.; Elias-Arnanz, M.,B-12-based photoreceptors: from structure and function to applications in optogenetics and synthetic biology. *Curr. Opin. Struct. Biol.* **2019**, *57*, 47-55, 10.1016/j.sbi.2019.01.020.

(35) Padmanabhan, S.; Jost, M.; Drennan, C. L.; Elias-Arnanz, M.,A new facet of vitamin B_{12}: Gene regulation by cobalamin-based photoreceptors. *Annu. Rev. Biochem.* **2017**, *86*, 485-514, 10.1146/annurev-biochem-061516-044500.

(36) Kutta, R. J.; Hardman, S. J. O.; Johannissen, L. O.; Bellina, B.; Messiha, H. L.; Ortiz-Guerrero, J. M.; Elias-Arnanz, M.; Padmanabhan, S.; Barran, P.; Scrutton, N. S.; Jones, A. R.,The photochemical mechanism of a B_{12}-dependent photoreceptor protein. *Nat. Commun.* **2015**, *6*, 7907, 10.1038/ncomms8907.

(37) Jost, M.; Simpson, J. H.; Drennan, C. L.,The transcription factor CarH safeguards use of adenosylcobalamin as a light sensor by altering the photolysis products. *Biochemistry* **2015**, *54*, 3231-3234, 10.1021/acs.biochem.5b00416.

(38) Jost, M.; Fernandez-Zapata, J.; Polanco, M. C.; Ortiz-Guerrero, J. M.; Chen, P. Y. T.; Kang, G.; Padmanabhan, S.; Elias-Arnanz, M.; Drennan, C. L.,Structural basis for gene regulation by a B_{12}-dependent photoreceptor. *Nature* **2015**, *526*, 536-541, 10.1038/nature14950.

(39) Vogler, A.; Hirschmann, R.; Otto, H.; Kunkley, H.,Photochemistry of biologically important transition-metal complexes .1. Cyanocobalamin and related corrin complexes of rhodium(III). *Ber. Bunsenges. Phys. Chem.* **1976**, *80*, 420-424, 10.1002/bbpc.19760800506.

(40) Harris, D. A.; Stickrath, A. B.; Carroll, E. C.; Sension, R. J.,Influence of environment on the electronic structure of cob(III)alamins: Time-resolved absorption studies of the S_1 state spectrum

and dynamics. *J. Am. Chem. Soc.* **2007**, *129*, 7578-7585, 10.1021/ja066197y.

(41) Shiang, J. J.; Cole, A. G.; Sension, R. J.; Hang, K.; Weng, Y.; Trommel, J. S.; Marzilli, L. G.; Lian, T.,Ultrafast Excited-State Dynamics in Vitamin B_{12} and Related Cob(III)Alamins. *J. Am. Chem. Soc.* **2006**, *128*, 801-808, 10.1021/ja054374+.

(42) Wiley, T. E.; Miller, W. R.; Miller, N. A.; Sension, R. J.; Lodowski, P.; Jaworska, M.; Kozlowski, P. M.,Photostability of hydroxocobalamin: Ultrafast excited state dynamics and computational studies. *J. Phys. Chem. Lett.* **2016**, *7*, 143-147, 10.1021/acs.jpclett.5b02333.

(43) Dragnea, V.; Gonzalez-Gutierrez, G.; Bauer, C. E.,Structural Analyses of CrtJ and Its B-12-Binding Co-Regulators SAerR and LAerR from the Purple Photosynthetic Bacterium Rhodobacter capsulatus. *MICROORGANISMS* **2022**, *10*, 912, 10.3390/microorganisms10050912.

(44) Yamamoto, H.; Fang, M. X.; Dragnea, V.; Bauer, C. E.,Differing isoforms of the cobalamin binding photoreceptor AerR oppositely regulate photosystem expression. *ELIFE* **2018**, *7*, 10.7554/eLife.39028.

(45) Fang, M.; Bauer, C. E.,The Vitamin B12-Dependent Photoreceptor AerR Relieves Photosystem Gene Repression by Extending the Interaction of CrtJ with Photosystem Promoters. *mBio* **2017**, *8*, e00261-00217, 10.1128/mBio.00261-17.

(46) Cheng, Z.; Yamamoto, H.; Bauer, C. E.,Cobalamin's (Vitamin B-12) Surprising Function as a Photoreceptor. *Trends Biochem Sci* **2016**, *41*, 647-650, 10.1016/j.tibs.2016.05.002.

(47) Kainrath, S.; Stadler, M.; Reichhart, E.; Distel, M.; Janovjak, H.,Green-light-induced inactivation of receptor signaling using cobalamin-binding domains. *Angew. Chem., Int. Ed.* **2017**, *56*, 4608-4611, 10.1002/anie.201611998.

(48) Zobi, F.; Quaroni, L.; Santoro, G.; Zlateva, T.; Blacque, O.; Sarafimov, B.; Schaub, M. C.; Bogdanova, A. Y.,Live-Fibroblast IR Imaging of a Cytoprotective PhotoCORM Activated with

Visible Light. *J. Med. Chem.* **2013**, *56*, 6719-6731, 10.1021/jm400527k.

(49) Zobi, F.; Blacque, O.; Jacobs, R. A.; Schaub, M. C.; Bogdanova, A. Y.,17 e(-) rhenium dicarbonyl CO-releasing molecules on a cobalamin scaffold for biological application. *Dalton Trans.* **2012**, *41*, 370-378, 10.1039/c1dt10649j.

(50) Kinschel, D.; Bacellar, C.; Cannelli, O.; Sorokin, B.; Katayama, T.; Mancini, G. F.; Rouxel, J. R.; Obara, Y.; Nishitani, J.; Ito, H.; Ito, T.; Kurahashi, N.; Higashimura, C.; Kudo, S.; Keane, T.; Lima, F. A.; Gawelda, W.; Zalden, P.; Schulz, S.; Budarz, J. M.; Khakhulin, D.; Galler, A.; Bressler, C.; Milne, C. J.; Penfold, T.; Yabashi, M.; Suzuki, T.; Misawa, K.; Chergui, M.,Femtosecond X-ray emission study of the spin cross-over dynamics in haem proteins. *Nat. Commun.* **2020**, *11*, 4145, 10.1038/s41467-020-17923-w.

(51) Ledbetter, K.; Reinhard, M. E.; Kunnus, K.; Gallo, A.; Britz, A.; Biasin, E.; Glownia, J. M.; Nelson, S.; Van Driel, T. B.; Weninger, C.; Zederkof, D. B.; Haldrup, K.; Cordones, A. A.; Gaffney, K. J.; Sokaras, D.; Alonso-Mori, R.,Excited state charge distribution and bond expansion of ferrous complexes observed with femtosecond valence-to-core x-ray emission spectroscopy. *J. Chem. Phys.* **2020**, *152*, 074203, 10.1063/1.5139441.

(52) Kunnus, K.; Vacher, M.; Harlang, T. C. B.; Kjær, K. S.; Haldrup, K.; Biasin, E.; van Driel, T. B.; Pápai, M.; Chabera, P.; Liu, Y.; Tatsuno, H.; Timm, C.; Källman, E.; Delcey, M.; Hartsock, R. W.; Reinhard, M. E.; Koroidov, S.; Laursen, M. G.; Hansen, F. B.; Vester, P.; Christensen, M.; Sandberg, L.; Németh, Z.; Szemes, D. S.; Bajnóczi, É.; Alonso-Mori, R.; Glownia, J. M.; Nelson, S.; Sikorski, M.; Sokaras, D.; Lemke, H. T.; Canton, S. E.; Møller, K. B.; Nielsen, M. M.; Vankó, G.; Wärnmark, K.; Sundström, V.; Persson, P.; Lundberg, M.; Uhlig, J.; Gaffney, K. J.,Vibrational wavepacket dynamics in Fe carbene photosensitizer determined with femtosecond X-ray emission and scattering. *Nat. Commun.* **2020**, *11*, 634, 10.1038/s41467-020-14468-w.

(53) Cammarata, M.; Zerdane, S.; Balducci, L.; Azzolina, G.; Mazerat, S.; Exertier, C.; Trabuco, M.; Levantino, M.; Alonso-Mori, R.; Glownia, J. M.; Song, S.; Catala, L.; Mallah, T.; Matar, S. F.; Collet, E.,Charge transfer driven by ultrafast spin transition in a CoFe Prussian blue analogue. *Nat. Chem.* **2021**, *13*, 10-14, 10.1038/s41557-020-00597-8.

(54) Lemke, H. T.; Kjaer, K. S.; Hartsock, R.; van Driel, T. B.; Chollet, M.; Glownia, J. M.; Song, S.; Zhu, D. L.; Pace, E.; Matar, S. F.; Nielsen, M. M.; Benfatto, M.; Gaffney, K. J.; Collet, E.; Cammarata, M.,Coherent Structural Trapping Through Wave Packet Dispersion During Photoinduced Spin State Switching. *Nat. Commun.* **2017**, *8*, 15342, 15342 10.1038/ncomms15342.

(55) Canton, S. E.; Kjaer, K. S.; Vanko, G.; van Driel, T. B.; Adachi, S. I.; Bordage, A.; Bressler, C.; Chabera, P.; Christensen, M.; Dohn, A. O.; Galler, A.; Gawelda, W.; Gosztola, D.; Haldrup, K.; Harlang, T.; Liu, Y. Z.; Moller, K. B.; Nemeth, Z.; Nozawa, S.; Papai, M.; Sato, T.; Suarez-Alcantara, K.; Togashi, T.; Tono, K.; Uhlig, J.; Vithanage, D. A.; Warnmark, K.; Yabashi, M.; Zhang, J. X.; Sundstrom, V.; Nielsen, M. M.,Visualizing the non-equilibrium dynamics of photoinduced intramolecular electron transfer with femtosecond X-ray pulses. *Nat. Commun.* **2015**, *6*, 6359 6359 10.1038/ncomms7359.

(56) Canton, S. E.; Biednov, M.; Pápai, M.; Lima, F. A.; Choi, T.-K.; Otte, F.; Jiang, Y.; Frankenberger, P.; Knoll, M.; Zalden, P.; Gawelda, W.; Rahaman, A.; Møller, K. B.; Milne, C.; Gosztola, D. J.; Zheng, K.; Retegan, M.; Khakhulin, D.,Ultrafast Jahn-Teller Photoswitching in Cobalt Single-Ion Magnets. *Adv. Sci.* **2023**, 2206880, 10.1002/advs.202206880.

(57) Neese, F.,Software update: The ORCA program system—Version 5.0. *WIREs Comput. Mol. Sci.* **2022**, *12*, e1606, 10.1002/wcms.1606.

(58) Geoghegan, B. L.; Liu, Y.; Peredkov, S.; Dechert, S.; Meyer, F.; DeBeer, S.; Cutsail, G. E., III,Combining Valence-to-Core X-ray Emission and Cu K-edge X-ray Absorption Spectroscopies to Experimentally Assess Oxidation State in Organometallic Cu(I)/(II)/(III) Complexes. *J. Am. Chem. Soc.* **2022**, *144*, 2520-2534, 10.1021/jacs.1c09505.

(59) McCubbin Stepanic, O.; Ward, J.; Penner-Hahn, J. E.; Deb, A.; Bergmann, U.; DeBeer, S.,Probing a Silent Metal: A Combined X-ray Absorption and Emission Spectroscopic Study of Biologically Relevant Zinc Complexes. *Inorg. Chem.* **2020**, *59*, 13551-13560, 10.1021/acs.inorgchem.0c01931.

(60) Roemelt, M.; Beckwith, M. A.; Duboc, C.; Collomb, M.-N.; Neese, F.; DeBeer, S.,Manganese K-Edge X-Ray Absorption Spectroscopy as a Probe of the Metal–Ligand Interactions in Coordination Compounds. *Inorg. Chem.* **2012**, *51*, 680-687, 10.1021/ic202229b.

(61) Peng, G.; deGroot, F. M. F.; Haemaelaeinen, K.; Moore, J. A.; Wang, X.; Grush, M. M.; Hastings, J. B.; Siddons, D. P.; Armstrong, W. H.,High-resolution manganese x-ray fluorescence spectroscopy. Oxidation-state and spin-state sensitivity. *J. Am. Chem. Soc.* **1994**, *116*, 2914-2920, 10.1021/ja00086a024.

(62) Stich, T. A.; Brooks, A. J.; Buan, N. R.; Brunold, T. C.,Spectroscopic and computational studies of Co^{3+}-corrinoids: Spectral and electronic properties of the B_{12} cofactors and biologically relevant precursors. *J. Am. Chem. Soc.* **2003**, *125*, 5897-5914, 10.1021/ja029328d.

(63) Bunau, O.; Joly, Y.,Self-consistent aspects of X-ray absorption calculations. *J. Phys. Condens. Matter* **2009**, *21*, 345501, 10.1088/0953-8984/21/34/345501.

(64) Joly, Y.,X-ray absorption near-edge structure calculations beyond the muffin-tin approximation. *Phys. Rev. B* **2001**, *63*, 125120, 10.1103/PhysRevB.63.125120.

(65) Kratky, C.; Farber, G.; Gruber, K.; Wilson, K.; Dauter, Z.; Nolting, H.-F.; Konrat, R.;

Kräutler, B.,Accurate structural data demystify B12: High-resolution solid-state structure of aquocobalamin perchlorate and structure analysis of the aquocobalamin ion in solution. *J. Am. Chem. Soc.* **1995**, *117*, 4654-4670,

(66) Ouyang, L. Z.; Rulis, P.; Ching, W. Y.; Slouf, M.; Nardin, G.; Randaccio, L.,Electronic structure and bonding in hydroxocobalamin. *Spectroc. Acta Pt. A-Molec. Biomolec. Spectr.* **2005**, *61*, 1647-1652,

(67) Widner, F. J.; Kieninger, C.; Wurst, K.; Deery, E.; Lawrence, A. D.; Warren, M. J.; Kräutler, B.,Synthesis, Spectral Characterization and Crystal Structure of Chlororhodibalamin: A Synthesis Platform for Rhodium Analogues of Vitamin B12 and for Rh-Based Antivitamins B12. *Synthesis* **2020**, *53*, 332-337, 10.1055/s-0040-1707288.

(68) Lafuerza, S.; Carlantuono, A.; Retegan, M.; Glatzel, P.,Chemical Sensitivity of Kβ and Kα X-ray Emission from a Systematic Investigation of Iron Compounds. *Inorg. Chem.* **2020**, *59*, 12518-12535, 10.1021/acs.inorgchem.0c01620.

(69) Pollock, C. J.; Delgado-Jaime, M. U.; Atanasov, M.; Neese, F.; DeBeer, S.,Kβ Mainline X-ray Emission Spectroscopy as an Experimental Probe of Metal–Ligand Covalency. *J. Am. Chem. Soc.* **2014**, *136*, 9453-9463, 10.1021/ja504182n.

(70) Vankó, G.; Neisius, T.; Molnár, G.; Renz, F.; Kárpáti, S.; Shukla, A.; de Groot, F. M. F.,Probing the 3d Spin Momentum with X-ray Emission Spectroscopy: The Case of Molecular-Spin Transitions. *J. Phys. Chem. B* **2006**, *110*, 11647-11653, 10.1021/jp0615961.

(71) Chollet, M.; Alonso-Mori, R.; Cammarata, M.; Damiani, D.; Defever, J.; Delor, J. T.; Feng, Y. P.; Glownia, J. M.; Langton, J. B.; Nelson, S.; Ramsey, K.; Robert, A.; Sikorski, M.; Song, S.; Stefanescu, D.; Srinivasan, V.; Zhu, D. L.; Lemke, H. T.; Fritz, D. M.,The X-ray pump-probe instrument at the Linac Coherent Light Source. *J. Synchrot. Radiat.* **2015**, *22*, 503-507,

10.1107/S1600577515005135.

(72) Michocki, L. B.; Miller, N. A.; Alonso-Mori, R.; Britz, A.; Deb, A.; Glownia, J. M.; Kaneshiro, A. K.; Konar, A.; Meadows, J. H.; Sofferman, D. L.; Song, S.; Toda, M. J.; van Driel, T. B.; Kozlowski, P. M.; Kubarych, K. J.; Penner-Hahn, J. E.; Sension, R. J.,Probing the excited state of methylcobalamin using polarized time-resolved X-ray absorption spectroscopy. *J. Phys. Chem. B* **2019**, *123*, 6042-6048, 10.1021/acs.jpcb.9b05854.

(73) Weng, T.-C.; Waldo, G. S.; Penner-Hahn, J. E.,A method for normalization of X-ray absorption spectra. *J. Synchrot. Radiat.* **2005**, *12*, 506-510, 10.1107/S0909049504034193.

(74) Khakhulin, D.; Otte, F.; Biednov, M.; Bömer, C.; Choi, T.-K.; Diez, M.; Galler, A.; Jiang, Y.; Kubicek, K.; Lima, F. A.; Rodriguez-Fernandez, A.; Zalden, P.; Gawelda, W.; Bressler, C.,Ultrafast X-ray Photochemistry at European XFEL: Capabilities of the Femtosecond X-ray Experiments (FXE) Instrument. *Applied Sciences* **2020**, *10*, 995, 10.3390/app10030995.

(75) Galler, A.; Gawelda, W.; Biednov, M.; Bomer, C.; Britz, A.; Brockhauser, S.; Choi, T.-K.; Diez, M.; Frankenberger, P.; French, M.; Gorries, D.; Hart, M.; Hauf, S.; Khakhulin, D.; Knoll, M.; Korsch, T.; Kubicek, K.; Kuster, M.; Lang, P.; Alves Lima, F.; Otte, F.; Schulz, S.; Zalden, P.; Bressler, C.,Scientific instrument Femtosecond X-ray Experiments (FXE): instrumentation and baseline experimental capabilities. *J. Synchrot. Radiat.* **2019**, *26*, 1432-1447, 10.1107/S1600577519006647.

(76) Decking, W.; Abeghyan, S.; Abramian, P.; Abramsky, A.; Aguirre, A.; Albrecht, C.; Alou, P.; Altarelli, M.; Altmann, P.; Amyan, K.; Anashin, V.; Apostolov, E.; Appel, K.; Auguste, D.; Ayvazyan, V.; Baark, S.; Babies, F.; Baboi, N.; Bak, P.; Balandin, V.; Baldinger, R.; Baranasic, B.; Barbanotti, S.; Belikov, O.; Belokurov, V.; Belova, L.; Belyakov, V.; Berry, S.; Bertucci, M.; Beutner, B.; Block, A.; Blöcher, M.; Böckmann, T.; Bohm, C.; Böhnert, M.; Bondar, V.;

Bondarchuk, E.; Bonezzi, M.; Borowiec, P.; Bösch, C.; Bösenberg, U.; Bosotti, A.; Böspflug, R.; Bousonville, M.; Boyd, E.; Bozhko, Y.; Brand, A.; Branlard, J.; Briechle, S.; Brinker, F.; Brinker, S.; Brinkmann, R.; Brockhauser, S.; Brovko, O.; Brück, H.; Brüdgam, A.; Butkowski, L.; Büttner, T.; Calero, J.; Castro-Carballo, E.; Cattalanotto, G.; Charrier, J.; Chen, J.; Cherepenko, A.; Cheskidov, V.; Chiodini, M.; Chong, A.; Choroba, S.; Chorowski, M.; Churanov, D.; Cichalewski, W.; Clausen, M.; Clement, W.; Cloué, C.; Cobos, J. A.; Coppola, N.; Cunis, S.; Czuba, K.; Czwalinna, M.; D'Almagne, B.; Dammann, J.; Danared, H.; de Zubiaurre Wagner, A.; Delfs, A.; Delfs, T.; Dietrich, F.; Dietrich, T.; Dohlus, M.; Dommach, M.; Donat, A.; Dong, X.; Doynikov, N.; Dressel, M.; Duda, M.; Duda, P.; Eckoldt, H.; Ehsan, W.; Eidam, J.; Eints, F.; Engling, C.,A MHz-repetition-rate hard X-ray free-electron laser driven by a superconducting linear accelerator. *Nature Photonics* **2020**, *14*, 391-397, 10.1038/s41566-020-0607-z.